



Electrocatalysts and components for polymer-based composite films: pyrolytic carbon deposited on metal and metal oxides derived from hydrotalcite-like materials

Aleksandra Pacuła^{1,*}, Jacek Gurgul¹, Robert P. Socha¹, Piotr Pietrzyk², Małgorzata Ruggiero-Mikołajczyk¹, Dorota Duraczyńska¹, Marcel Krzan¹, Małgorzata Nattich-Rak¹, Grzegorz Mordarski¹, Jan Żukrowski³, Marta Sadowska¹, and Bogna D. Napruszewska¹

¹ Jerzy Haber Institute of Catalysis and Surface Chemistry, Polish Academy of Sciences, Niezapominajek 8, 30-239 Kraków, Poland

² Faculty of Chemistry, Jagiellonian University, Gronostajowa 2, 30-387 Kraków, Poland

³ Academic Centre for Materials and Nanotechnology, AGH University of Science and Technology, Mickiewicza 30, 30-059 Kraków, Poland

Received: 24 January 2025

Accepted: 2 June 2025

© The Author(s), 2025

ABSTRACT

N- and Fe-containing carbon-based materials were prepared at 600 and 700 °C via catalytic chemical vapor deposition (CCVD) with acetonitrile (as carbon and nitrogen source) with the application of metal/metal oxides generated in situ from Mg–Fe–Al hydrotalcite-like materials (HTs). The impact of synthesis temperature and transition metal (Fe) concentration in a blend of metal oxides derived from HTs on carbon deposit content and its structural ordering, nitrogen doping, location of N-containing groups in graphitic array, morphology and porosity was investigated using XRD, EA, XRF, XPS, SEM, HR-TEM, Raman and Mössbauer spectroscopy, and N₂ sorption. Higher synthesis temperature and increased concentration of Fe-containing species occurring in a mixture of metal oxides derived from Mg–Fe–Al HTs enhanced the quantity of carbonaceous product, the mesopore volume and the thickness of graphitic domains occurring in the carbon materials and lowered nitrogen doping extent in carbon framework. Enhanced accessibility to active sites via pore network, as well as, improved electrical conductivity associated with increased graphitic domain thickness and reduced amorphous carbon content were found to be critical factors in their performance for oxygen reduction reaction (ORR) in alkaline electrolyte. No direct correlation between the population of N-containing species and ORR activity is observed but the presence of quaternary N appears to enhance selectivity for the 4-electron pathway. In addition, the influence of the carbon materials dispersed in polymer matrix in polycaprolactone (PCL)-based composite films on bulk (conductivity,

Handling Editor: Biao Chen.

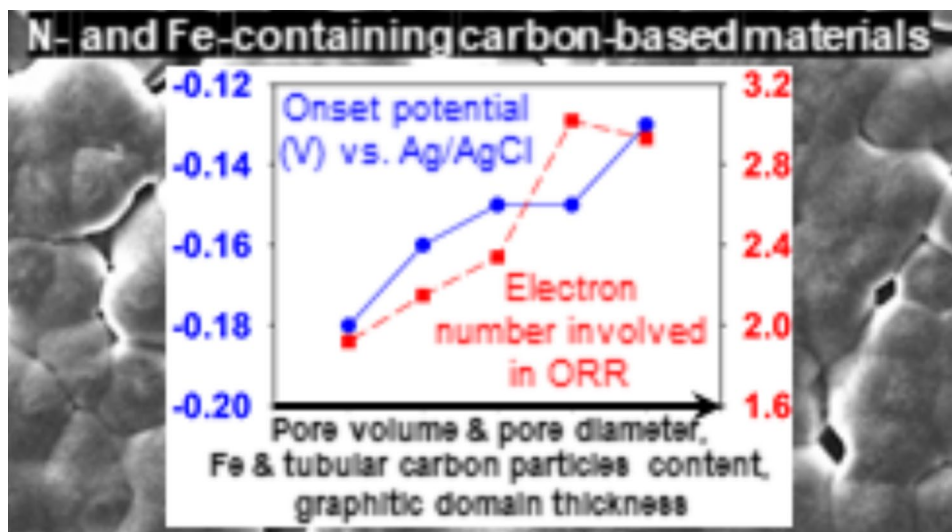
Address correspondence to E-mail: aleksandra.pacula@ikifp.edu.pl

<https://doi.org/10.1007/s10853-025-11081-4>

Published online: 26 June 2025

dielectric constant) and surface (morphology, topography, roughness and water contact angle) properties was also described.

GRAPHICAL ABSTRACT



Introduction

The oxygen reduction reaction (ORR) plays a crucial role in numerous electrochemical devices, such as fuel cells, which directly convert chemical energy into electrical energy. ORR can proceed via two possible 2- or 4-electron reaction pathways. To date, platinum (Pt)-based catalysts have been recognized as the most efficient materials for catalyzing the 4-electron O_2 reduction. However, due to the high cost of Pt and its limited availability, extensive research has been dedicated to developing alternative catalysts for ORR. This global effort aims to reduce reliance on Pt while maintaining or improving the performance of ORR in electrochemical devices.

Doping carbon materials with nitrogen (N) has garnered significant attention for the development of electrocatalysts for ORR, especially in alkaline electrolytes, as potential replacement for Pt-based catalysts [1–4]. Nitrogen inserted in carbon matrix is responsible for the creation of the active sites for ORR, as high electron affinity of nitrogen atom can produce a positive charge density into the adjacent carbon atom, which facilitates easier oxygen adsorption. The catalytic active sites are the neighbor carbon atoms where oxygen molecule is attracted, chemisorbed and then reduced.

Based on the review [3] and references therein, pyridinic N is the most reported as responsible for the high activity of N-doped carbon materials. DFT calculations showed that the chemisorption of molecular oxygen on the carbon atom adjacent to the pyridinic N at armchair position is more favorable compared to the carbon atom adjacent to the pyridinic N located at zigzag position. Besides, pyrrolic N and quaternary (or graphitic) N are considered as functionalities responsible for the formation of catalytic active sites. DFT calculations showed that the chemisorption of oxygen molecule on the sites created by edge-type graphitic N is more favorable than by the carbon atom next to basal-type quaternary N.

Among various carbon (C) and nitrogen (N) precursors, acetonitrile (CH_3CN) is considered an efficient dual-source of C and N for the synthesis of N-doped carbon materials via chemical vapor deposition (CVD) or catalytic CVD (CCVD). As noted in the book *Enhanced Carbon-Based Materials and Their Applications* [5], CVD/CCVD is widely regarded as a prominent method for producing carbon nanostructures. Drawing on our extensive experience in the synthesis of N-doped carbon materials from CH_3CN using hydrotalcite-like materials (HTs) as catalyst/support precursors—previously evaluated for hydrogen storage, charge storage, electrocatalysis (e.g., methanol oxidation), and as catalyst supports [6–9]—we applied

a similar approach to produce N-doped carbon materials for evaluation their electrochemical properties in alkaline medium with the addition of oxygen as a probe molecule.

The use of CH_3CN vapor as a C/N precursor for the preparation of ORR electrocatalysts began approximately 25 years ago, with pioneering work by Dodelet and colleagues [10–13]. They synthesized electrocatalysts by carbonizing CH_3CN vapor at various temperatures: 600–1000 °C for 1–2 h in the presence of 2% Fe/C or 10% Fe/C, utilizing various organic compounds as Fe precursors. For instance, the electrocatalysts obtained at 1000 °C for 1 h derived from 2% Fe/C contained Fe and N at concentrations of 0.2 and 4.8 at.%, respectively, while the electrocatalysts derived from 10% Fe/C contained Fe and N at concentrations of 9.9 and 6.1 at.%, respectively. The iron existed as Fe-containing species (Fe^0 , Fe^{2+} , Fe^{3+}) but not as Fe- N_x species. The presence of N-containing groups (pyridinic N, pyrrolic N, graphitic N, and oxidized N) was confirmed in those materials. The resulting materials, initially without any further purification and subsequently with treatment with acid, demonstrated both activity and stability in ORR within an acidic electrolyte. Based on their results, Fe-containing particles did not exhibit catalytic activity. Furthermore, the catalytic performance was attributed to the presence of N-containing groups (pyridinic N, pyrrolic N, and graphitic N).

Since 2006, Ozkan and her colleagues have made significant strides in developing electrocatalysts derived from CH_3CN vapor for ORR [14–22]. Their initial studies focused on synthesizing a series of electrocatalysts by pyrolyzing CH_3CN vapor at temperatures of 600–900 °C in the presence of Fe or Ni deposited on Vulcan carbon (VC) using appropriate acetate salts as metal precursors [14]. The nominal content of transition metals in the supported catalysts was 2 wt%. In addition, they studied the effects of varying pyrolysis times (20 min, 2 h, and 12 h). Then, they extended their work by carbonizing CH_3CN vapor at 900 °C for 2 h in the presence of 2% Fe or Ni supported on Al_2O_3 [15]. They also examined the effect of increasing Fe content from 2 up to 10% in the Fe/ Al_2O_3 system [16]. However, increasing Fe concentration did not improve ORR performance.

Ozkan and her team also investigated the use of alternative supports, such as SiO_2 and MgO , for the preparation of electrocatalysts [17, 18]. They carried out the pyrolysis of CH_3CN vapor at 900 °C for 2 h

using Fe, Co, and Ni salts as impregnating agents, with a nominal transition metal concentration of 2 wt%. After impregnation, the supports were further heated at 550 °C under H_2 flow. To compare, they also pyrolyzed CH_3CN vapor using the pure supports. The carbon deposit morphology varied significantly between Fe-, Co- and Ni-containing catalysts. The presence of Fe and Co on the supports resulted in the formation of carbon nanofibers (CNFs) with a stacked-cup structure, whereas supported Ni led to the formation of MWCNTs or broken MWCNTs. These carbon nanostructures contained a relatively high amount of metal particles encapsulated inside. Fe-containing phases present in electrocatalysts derived from CH_3CN pyrolysis over supported metal particles included metallic Fe, cementite, and oxidized Fe. Acid washing removed more of the carbide and oxidized phases, leaving behind metallic Fe. There was no clear correlation between the activity and the iron phases present. The findings suggested that iron's role in these catalysts was to facilitate the formation of carbon nanostructures, which increased edge-plane exposure and potentially the number of nitrogen functional groups on the surface. The resulting materials, initially without any further purification and subsequently with treatment using acid or base, were examined for their ORR performance in acidic medium. The highest ORR activity was observed for N-doped carbon nanostructures (CN_x) grown on Fe and Co supported catalysts. The purification led to a modest improvement in ORR activity, likely due to the removal of inactive supports and exposed metal. Further analysis revealed that increasing pyridinic N content and edge-plane exposure enhanced catalytic performance. The authors speculated that pyridinic N itself may not serve as the active site but instead acts as an indicator of exposed edge planes.

Next, the authors evaluated the effect of increasing Co content from 2 up to 10% in the Co/ MgO and Co/VC systems on CN_x obtained by carbonizing CH_3CN at 800 °C for 2 h [21]. The synthesized materials were treated with HCl to remove the metal carbide phase and MgO , leaving only CN_x with cobalt particles encapsulated within the carbon nanostructures. The cobalt phase in both acid-treated samples was predominantly metallic (Co^0) compared to oxidized (Co^{2+}). Both as-prepared and acid-treated materials were tested for ORR in acidic medium. Acid treatment improved electrocatalytic performance compared to unwashed samples, although the selectivity remained

similar. CN_x grown over MgO exhibited a higher content of pyridinic N than those grown over VC. The catalyst derived from 10% Co/MgO showed higher activity than that derived from 10% Co/VC, with differences in ORR activity being partially attributed to variations in pyridinic N content.

In conclusion, the literature data demonstrate that the metal itself is not the primary factor driving electrocatalytic activity. No evidence was found to support the involvement of N-coordinated active metal sites in ORR. Specifically, iron, being encapsulated within the carbon nanostructures, does not directly contribute to the active site for ORR. Instead, iron likely plays a role in the formation of the active site during the growth of carbon nanostructures, enhancing edge-plane exposure and potentially increasing the number of N-containing functional groups on the surface. These findings underscore the significance of the carbon nanostructure architecture and nitrogen content in determining electrocatalytic performance. The authors emphasized that the presence of pyridinic N and the degree of graphitic edge plane exposure are critical factors influencing ORR performance. Based on the available literature, the use of Al_2O_3 and MgO as supports for transition metals has demonstrated considerable advantages in synthesizing N-doped carbon materials with desirable properties. These materials exhibit relatively high specific surface areas, elevated nitrogen content, and a significant concentration of graphitic edge planes, all of which enhance their ORR activity.

Since 2007, Fe-containing HTs have been explored for synthesizing N-doped carbon materials. Early work by Chinese researchers, including Zhao et al., used $Mg_2Fe_{0.1}Al_{0.9}$, $Zn_2Fe_{0.1}Al_{0.9}$, and $Cu_2Fe_{0.1}Al_{0.9}$ HTs to produce SWCNTs and MWCNTs via calcination and reduction at 600 °C, followed by CH_4 -based CVD at 900 °C [23]. In 2010, MgFe HTs enabled N-doped CNT growth using ethylenediamine as a nitrogen source at 550–750 °C [24].

From 2010, Wei et al. at Tsinghua University systematically studied MgFeAl HTs, varying synthesis conditions (750–900 °C) and precursors (CH_4 , C_2H_4 , CH_3CN) to yield SWCNTs and N-doped CNTs [25–28]. Their work progressed to graphene/SWCNT hybrids, synthesized via CH_4 carbonization at 900–1000 °C for 10–15 min using metal/metal oxide catalysts from $Mg_{3.0}Fe_{0.4}Al_{1.0}$ and $Mg_{1.6-1.9}Fe_{0.6-0.83}Al_{1.0}$ HTs.

Previous studies have underscored the critical roles of temperature, pyrolysis duration, and active species

concentration in determining the structure of carbon deposits, the formation of carbon nanostructures, and the extent of nitrogen doping. Fe-containing HTs are particularly advantageous precursors for CCVD-based carbon synthesis. Incorporation of Fe^{3+} ions into the HT lattice—coordinated with divalent (e.g., Mg^{2+}) and trivalent cations (e.g., Al^{3+})—ensures uniform dispersion of iron species, including iron oxides and partially reduced forms, as well as metallic iron on the surface of the resulting metal oxide mixture. These metallic iron nanoparticles (NPs) serve as effective catalysts for carbon nanostructure growth. Additionally, the amorphous Al_2O_3 phase formed during HT decomposition helps prevent Fe NP agglomeration, thereby enhancing their dispersion and catalytic performance.

Iron atoms embedded within N-doped carbon frameworks may also contribute to improved ORR performance [29–32]. Like other transition metals such as cobalt or nickel, iron can serve as anchoring sites for Pt NPs, promoting their dispersion [33–36]. This high dispersion enables the use of low Pt loadings (~ 5 wt%) while still achieving strong catalytic activity. Such systems have demonstrated superior performance and stability in electrochemical reactions, including ORR and the hydrogen evolution reaction (HER), when compared to commercial Pt/C catalysts containing 20 wt% Pt.

Our previous research on MgCoAl and MgFeAl HTs [9, 37] confirmed the effectiveness of HT-derived Co or Fe nanoparticles as catalysts and Al_2O_3 /MgO as supports for CH_3CN carbonization, enabling the synthesis of N-doped carbon nanostructures. In a recent study [9], we reported the preparation of N-doped carbon materials via extended pyrolysis (180 min) of CH_3CN using MgFeAl HTs and evaluated their performance as capacitors and catalyst supports. In contrast, the present work focuses on materials synthesized under shorter pyrolysis conditions (30 min). The electroreduction of oxygen, one of the most extensively studied electrochemical processes, was selected to evaluate the electrocatalytic properties of synthetic carbon materials produced via CCVD/CVD using CH_3CN at 600 °C and 700 °C. These materials were synthesized in the presence of in situ-generated metal/metal oxide phases derived from Fe-containing HTs with varying iron content—classified as low (L), high (H), and very high (VH), and designated as MgFeAl-L, MgFeAl-H, and MgFeAl-VH, respectively.

Comprehensive physicochemical (XRD, EA, XRF, XPS, Raman, Mössbauer spectroscopy, N_2 sorption,

SEM, HR-TEM) and electrochemical (CV, LSV) analyses revealed enhanced ORR activity in the carbon materials synthesized at 700 °C compared to those prepared at 600 °C. This improvement is attributed to increased pore volume, broader pore size distribution—facilitating better access to active sites—and higher electrical conductivity, as evidenced by a lower amorphous carbon content and the development of thicker graphitic domains. The presence of CNTs also positively influenced ORR performance in N-doped carbon materials produced at both temperatures using Fe-containing HTs.

Interestingly, no direct correlation was observed between ORR activity or selectivity and the total nitrogen content in the carbon framework, despite N-functional groups traditionally being associated with improved ORR performance. However, synthesis at 700 °C, particularly with high or very high Fe content, promoted the formation of quaternary nitrogen species, which likely contribute to greater selectivity toward the four-electron ORR pathway.

Additionally, the study found no significant interaction between iron species encapsulated within the carbon matrix and the surrounding carbon structure, indicating limited catalytic synergy between these components. While the ORR activity of the resulting carbon materials is modest, the findings provide important insights into the structural, morphological, and porosity evolution of N- and Fe-doped carbon materials.

The primary aim of this work was not to optimize ORR performance but to understand how iron species derived from HTs influence the formation and characteristics of carbon deposits. The study also explores the potential of these Fe-containing carbon materials as supports for platinum, motivated by prior research showing that transition metals embedded in N-doped carbon matrices can serve as anchoring sites for Pt nanoparticles. Furthermore, the carbon materials were evaluated as components in polymer-based composite films.

Several review papers published between 2019 and 2022 [38–42] highlight the growing body of research focused on combining CNTs and their functionalized derivatives (f-CNTs) with biomaterials to develop novel, high-performance composites for bone repair and regeneration. Among various polymers, polycaprolactone (PCL) is widely used in tissue engineering due to its favourable rheological and viscoelastic properties, ease of processing, sufficient

mechanical strength, and biodegradability [43]. PCL is commonly employed in the fabrication of scaffolds designed to support cell growth. However, PCL lacks bioactive functional groups capable of eliciting cellular responses such as adhesion. To overcome this limitation, various carbon-based nanomaterials have been incorporated into PCL-based scaffolds, including elongated nanostructures such as CNTs, f-CNTs, carbon nanofibers (CNFs), and functionalized CNFs (f-CNFs) [44–46].

Scaffolds made from PCL/MWCNTs (3 wt%) and PCL/hydroxyapatite/MWCNTs (0.75 wt%) enhance hADSC attachment, proliferation, and differentiation even without electrical stimulation (ES) [47, 48]. Carbon-based additives improve mechanical strength, degradation, and introduce conductivity, which, while not essential, supports bone regeneration [49–51]. PCL/MWCNTs with ES promote thicker bone formation, angiogenesis, and mineralization [49]. PCL/hydroxyapatite/CNT (2 wt%) scaffolds balance mechanical and conductive properties, facilitating ES-driven healing. Higher CNT levels (up to 10 wt%) enhance protein adsorption and initial cell adhesion [50]. Surface-modified PCL/hydroxyapatite scaffolds with MWCNTs further improve conductivity, wettability, and bone cell proliferation and adhesion [51].

This study investigates the electrical and dielectric properties of PCL-based composite films incorporating the carbon materials. The effects of carbon addition on the crystalline structure of the PCL matrix, as well as the surface morphology and topography of the resulting composites, are systematically examined. The research is primarily fundamental in nature and does not include characterization of mechanical or biocompatibility properties of the composites.

Materials and methods

Materials

The chemicals including magnesium nitrate hexahydrate [Mg(NO₃)₂·6H₂O], iron (III) nitrate nonahydrate [Fe(NO₃)₃·9H₂O], aluminium nitrate nonahydrate [Al(NO₃)₃·9H₂O], sodium hydroxide [NaOH], potassium hydroxide [KOH], hydrochloric acid [HCl, 35–38%], acetonitrile [CH₃CN], *iso*-propyl alcohol [C₃H₇OH], chloroplatinic acid hexahydrate [H₂PtCl₆·6H₂O], sodium borohydride [NaBH₄], sodium citrate dihydrate [HOC(COONa)

(CH₂COONa)₂·2H₂O], poly(ϵ -caprolactone) denoted as PCL [M_n = 80 kDa], dichloromethane denoted as DCM were used as received. Commercial gases such as argon (Ar, 99.999%) and oxygen (O₂, 99.95%) were used in laboratory. Deionized water was obtained via Milli-Q purification system (Millipore).

Fabrication of the carbon materials

First, HTs varying in chemical compositions: MgFeAl-L HTs (Mg/Fe/Al = 3.0:0.2:0.8), MgFeAl-H HTs (Mg/Fe/Al = 3.0:0.4:0.6), MgFeAl-VH HTs (Mg/Fe/Al = 3.0:0.5:0.5) were synthesized according to protocol described in our previous publications [9, 52]. Then, the samples were prepared via the pyrolysis of CH₃CN vapor at 600 and 700 °C in the presence of metal (iron)/metal oxides (magnesia, alumina, and iron oxides) generated in situ from HTs. The carbonization process lasted 30 min. After that, the samples obtained in CCVD experiments were treated with hydrochloric acid solution (HCl/H₂O 2:1 v/v) for 24 h and ultrasonically agitated for 60 min to remove inorganic compounds such as metal/metal oxides, which were exposed and not encased in carbonaceous component (carbon deposit). Finally, the acid-treated samples were separated, washed with H₂O and finally dried at 50 °C.

In this work, the samples obtained directly from CCVD experiments are labelled “the composites”, while those obtained after treating the composites with HCl solution “the carbon materials”. The composites prepared at 600 or 700 °C, with the compounds generated from HTs of varied chemical compositions, i.e. MgFeAl-L, MgFeAl-H, and MgFeAl-VH, are further denoted as HTs-600-30 or HTs-700-30, respectively. The corresponding carbon materials are denoted as C-HTs-600-30 or C-HTs-700-30, respectively.

Fabrication of platinum (Pt) nanoparticles (NPs) and their deposition on the carbon material

Pt NPs were obtained via chemical reduction of platinum ions using NaBH₄ according to the procedure [53]. Metal NPs in aqueous suspension were electrostatically stabilized with the addition of sodium citrate, therefore the estimated via ELS zeta potential (ζ) was negative (-40 ± 4 mV, pH = 4.5). The mean value of hydrodynamic diameter (d_H) of Pt NPs estimated by DLS was equal to 9 ± 1 nm (Fig. S1). The deposition

of Pt NPs on the surface of the carbon material was performed by adsorption. It is worth noting that the carbon grains in aqueous suspension (with a concentration of 0.4 g dm⁻³) formed agglomerates showing a positive ζ (44 ± 2 mV, pH = 3.4), therefore the deposition of Pt NPs characterized by negative ζ , was additionally electrostatically assisted.

Fabrication of the PCL-based films

The PCL-based composite films were fabricated by incorporating the carbon materials into polymer matrix via the direct-blending method inspired by previously published procedures [54, 55]. First, the carbon material was dispersed in DCM (~ 10 ml, ~ 13.3 g) using a sonication probe (a stepped microtip with a diameter of 3 mm installed in 750 Watts ultrasonic processor: SONICS VCX 750) for 10 min (19 s pulse, 5 s pause, 30% amplitude). Afterwards, PCL (~ 0.74 g) was added into the carbon material/DCM dispersion and the slurry was agitated at room temperature for 24 h using a roller shaker until a uniform mixture was achieved. Subsequently, the mixture was immediately poured into the centre of a glass Petri dish (with a diameter of ~ 9.4 cm) and left in a fume hood overnight (at room temperature) to evaporate DCM. The Petri dishes were protected with a plastic (polyethylene (PE)) foil to prevent physical contamination like dust particles. Then, the resulting PCL-based films were dried in a vacuum oven at 50 °C for 48 h to remove completely DCM remnants. The content of carbon additive was equal to 2.4, 4.6 and 6.8 wt%. Control film containing only PCL (5 wt% in DCM) was also prepared for comparison.

Characterization of the physicochemical properties

X-ray diffraction (XRD), elemental analysis (EA), X-ray fluorescence (XRF) analysis, nitrogen (N₂) adsorption/desorption, Raman spectroscopy, X-ray photoelectron spectroscopy (XPS), ⁵⁷Fe Mössbauer spectroscopy, Fourier transform infrared (FT-IR) spectroscopy, dynamic light scattering (DLS), electrophoretic light scattering (ELS), scanning electron microscopy (SEM), transmission electron microscopy (TEM), atomic force microscopy (AFM), and water contact angle (WCA) measurements were employed to characterize the properties of the studied samples.

Detailed descriptions of these methods and techniques are provided in the Supplementary material file.

Characterization of the electrocatalytic properties

Electrochemical measurements were carried out using a PGSTAT204 potentiostat (Metrohm Autolab) in a conventional three-electrode configuration. A Pt wire served as the counter electrode, while an Ag/AgCl/KCl_{sat} electrode was used as the reference electrode. The working electrode was a glassy carbon (GC) disc with a 5 mm diameter. Prior to measurement, the GC electrode was polished with an aqueous alumina suspension on a polishing cloth, followed by ultrasonic cleaning in Milli-Q water and isopropanol. A 2.5 mg sample of the material under study was mixed ultrasonically for 20 min with a 1 wt% Nafion solution in a mixture of ethanol and n-propanol (500 μ l). Following this, 5 μ l of the resulting suspension was applied onto the GC disc, which was then dried at room temperature in air. The loading of the studied material on the GC electrode was 0.128 mg cm⁻². Cyclic voltammetry (CV) was performed at a scan rate of 10 mV s⁻¹ in an aqueous 0.1 M KOH solution. Linear polarization measurements were conducted at a sweep rate of 5 mV s⁻¹ using a rotating disc electrode (RDE) with a rotation rate ranging from 400 to 1600 rpm, in alkaline electrolyte either saturated with oxygen or bubbled with argon. The temperature of 0.1 M KOH (25 \pm 1 $^{\circ}$ C) was maintained by JULABO (ED-5) thermostat. All of the potentials are referred to Ag/AgCl/KCl_{sat}. The number of electrons involved in ORR in the presence of the studied materials was determined from the experimental data using the Levich equation:

$$i = 0.62 n F A D^{2/3} C v^{-1/6} \omega^{1/2} = B \omega^{1/2}$$

where i is the measured limiting current, n is the number of electrons transferred per oxygen molecule, F is the Faraday's constant (96,485 C mol⁻¹), A is the geometric electrode area (0.196 cm²), D and C are the diffusion coefficient of dissolved oxygen (1.9 \times 10⁻⁵ cm² s⁻¹) and the concentration of dissolved oxygen (1.2 \times 10⁻⁶ mol cm⁻³) in 0.1 M KOH, respectively; v is the kinematic viscosity of the electrolyte solution (0.01 cm² s⁻¹), and ω is the rotation rate (rad s⁻¹) [56].

Characterization of the electrical properties of the films

The electrical properties of PCL-based films, including electrical conductivity (σ) and dielectric constant (ϵ), were determined by measuring resistance and capacitance, respectively, using a parallel equivalent circuit model for the resistor and capacitor. These measurements were performed at room temperature in air using a two-point probe method with an LCR (Inductance–Capacitance–Resistance) digital meter (8101G, GW Instek), applying alternating current (AC) at a frequency of $\nu = 1$ kHz. The samples were placed between two flat, circular brass discs, aligned in a column within a Teflon holder. Prior to contacting the brass pucks with the films, the relevant surface (exposed to the film) was smoothed with abrasive paper and cleaned with isopropanol. The diameter of the brass pucks was approximately 4 cm, resulting in a contact area of 1.22×10^{-3} m². Measurements were taken at four different locations on each film, sandwiched between two brass discs connected to the LCR meter via Kelvin clips (two pairs of wires). Therefore, the data are presented as the mean values \pm standard deviation from four measurements. The average film thickness was measured at four locations on each film using a digital micrometer with a plate (Mitutoyo). The mean thickness of the films ranged approximately from 108×10^{-6} to 151×10^{-6} m.

Results and discussion

Physicochemical characterization of the composites

The X-ray diffraction (XRD) analysis of the composites (Fig. S2a and b) and the corresponding normalized XRD plots (Fig. S3a–e) with the stick pattern from the ICDD database (PDF 00–045–0946) for MgO reveals nine reflections characteristic of MgO in the 2θ range of 5–139 $^{\circ}$. Additionally, a reflection corresponding to MgAl₂O₄ (at $2\theta \sim 37^{\circ}$, PDF 00–021–1152) overlaps with reflections associated with iron species, namely FeO (at $2\theta \sim 36^{\circ}$, PDF 01–089–0687) and Fe₃O₄ (at $2\theta \sim 35^{\circ}$, PDF 00–019–0629), resulting in a broad reflection in the 2θ range of ~ 35 –37 $^{\circ}$. It is well established in the literature that the thermal decomposition of MgAl hydrotalcites (HTs), especially at high temperatures,

Table 1 The content of carbon deposit (calculated from elemental analysis) in the composites prepared at 600 and 700 °C via CCVD/CVD (30 min) with the compounds derived from MgFeAl-L HTs, MgFeAl-H HTs and MgFeAl-VH HTs

HTs	CVD temp. (°C)	Carbon deposit (wt%)	HTs	CVD temp. (°C)	Carbon deposit (wt%)
MgFeAl-L	600	9.8	MgFeAl-L	700	26.3
MgFeAl-H	600	26.4	MgFeAl-H	700	36.4
–	–	–	MgFeAl-VH	700	41.2

leads to a mixture of MgO and MgAl₂O₄ phases [57]. Conversely, Fe₂O₃, which forms from the thermal decomposition of Fe-containing HTs [58, 59], can be reduced by solid carbon via gaseous intermediates like CO and CO₂, following the Boudouard reaction (C+CO₂→2CO) [60]. This reduction process leads to the formation of FeO, which can be further reduced to metallic Fe, and in some cases, iron carbide (Fe₃C) can be formed. Fe₃O₄ is typically considered an intermediate phase in the reduction of Fe₂O₃ to FeO, as it represents a chemical mixture of Fe₂O₃ and FeO. The XRD data suggest that MgO is the predominant crystalline phase in the composites, with only minor contributions from MgAl₂O₄, FeO, and Fe₃O₄. Notably, Fe₂O₃, Fe, and Fe₃C are not detectable by XRD. This is likely due to the low concentration and small crystallite size of Fe-containing phases, which fall below the detection limit of XRD. Similarly, calcination of MgFeAl HTs results in the formation of MgO and MgAl₂O₄ (as detected by XRD) and Fe₂O₃ (as detected by XPS) [58].

During CVD/CCVD experiments, CH₃CN vapor undergoes carbonization with the assistance of compounds generated in situ from MgFeAl HTs. The carbon content in the composites obtained at 600 °C with MgFeAl-L and MgFeAl-H HTs was found to be 9.8 and 26.4 wt%, respectively, which are lower than the 26.3 and 36.4 wt% observed in the corresponding samples synthesized at 700 °C (Table 1). This indicates that the amount of carbon deposit increases with increasing pyrolysis temperature. Furthermore, varying the iron concentration in Fe-containing HTs significantly affects the quantity of carbon deposit formed during pyrolysis of CH₃CN vapor at both 600 and 700 °C. The use of MgFeAl-H HTs in the CVD/CCVD process

leads to higher carbon deposits at both temperatures compared to MgFeAl-L HTs. This can be attributed to an increased contribution of iron species, such as defective Fe_xO_y and potentially an increase in the concentration of metallic iron, despite the absence of Fe reflections in the XRD data. Literature reports suggest that iron nanoparticles (NPs) play a critical role in the formation of solid carbon when in contact with hydrocarbons [23, 61, 62].

The XRD analysis do not reveal any reflections associated with carbon deposits in the sample with the lowest carbon content (9.8 wt%). However, for the composites with higher carbon content (26.3–41.2 wt%), a broad reflection at 2θ ~ 25–26° is observed, corresponding to the (002) diffraction plane of graphite (PDF 04–014–0362). These findings indicate that the composites consist of a mixture of metal oxides (MgO, MgAl₂O₄, FeO, Fe₃O₄) and graphite-like carbon in varying proportions.

Physicochemical characterization of the carbon materials

The elemental analysis (EA) data (Table 2) reveal that the carbon materials contain carbonaceous component ranging from 81.9 to 94.0 wt%, resulting in an estimated inorganic residue content between 6.0 and 18.1 wt%. A higher contribution of the carbonaceous component is observed in the carbon materials synthesized at 700 °C compared to those prepared at 600 °C, with values of 94.0 and 93.7 wt% for the former and 81.9 and 90.1 wt% for the latter.

XRD patterns of the carbon materials (Fig. 1) exhibit two broad reflections with peaks at 2θ ~ 26° and ~ 44°, as well as a shoulder at 2θ ~ 80°, corresponding to the (002), (100), and (110) diffraction planes of a two-dimensional turbostratic carbon lattice, respectively [63, 64]. As shown in Fig. S4a–e, the reflections shift to smaller angles compared to those observed in reference graphite with a hexagonal structure (PDF 04–014–0362). This indicates that the interlayer distance (*d*) in the turbostratic carbon present in the studied materials is larger (*d*₀₀₂ ~ 0.341, 0.342, and 0.344 nm) than in graphite (*d*₀₀₂ ~ 0.338 nm). This increase in interlayer distance is a result of both the low pyrolysis temperature (600 or 700 °C) and the substitution of some carbon atoms with nitrogen atoms in the graphitic lattice, leading to distortion of the graphitic layers.

The decreasing degree of graphitization of the carbonaceous material with increasing nitrogen doping

Table 2 The composition (calculated from elemental analysis) of the carbon materials prepared at 600 and 700 °C via CCVD/CVD (30 min) with the compounds derived from MgFeAl-L HTs, MgFeAl-H HTs and MgFeAl-VH HTs

Sample	Elemental analysis (wt%)					
	C	N	H	N/C ^a	C+N+H	Inorganic residue ^b
C-MgFeAl-L-600-30	70.2	10.0	1.7	0.122	81.9	18.1
C-MgFeAl-L-700-30	90.3	2.8	0.9	0.027	94.0	6.0
C-MgFeAl-H-600-30	83.8	5.1	1.2	0.052	90.1	9.9
C-MgFeAl-H-700-30	90.1	2.1	1.5	0.020	93.7	6.3
C-MgFeAl-VH-700-30	86.4	3.4	1.5	0.033	91.3	8.7

^aAtomic ratio

^bMass percentages are the values obtained by subtraction of (C+N+H) from 100 wt%

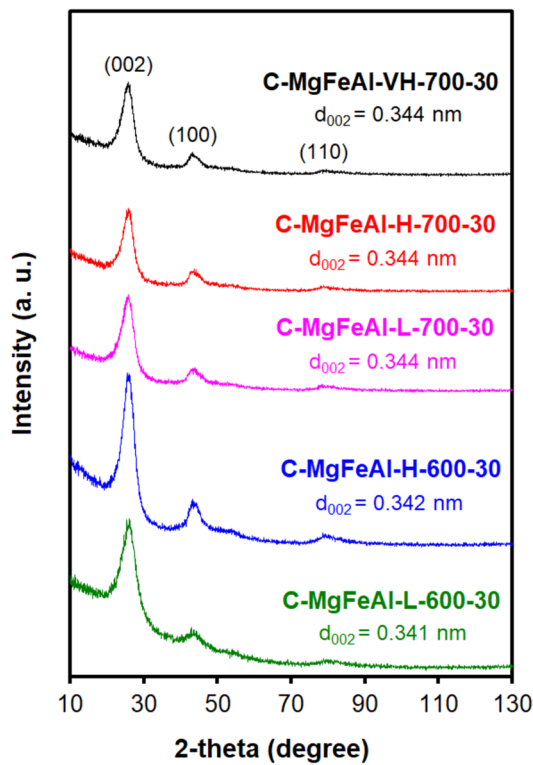


Figure 1 The XRD patterns of the carbon materials synthesized at 600 and 700 °C via CCVD/CVD in the presence of the compounds generated in situ from MgFeAl-L HTs, MgFeAl-H HTs and MgFeAl-VH HTs.

is further confirmed by Raman spectroscopy (Fig. 2). A more detailed analysis of the Raman spectra (Fig. S5a–e) reveals the information on the contributions of disordered carbon and amorphous carbon (Table 3). Details of the decomposition of Raman bands of the carbonaceous materials, attribution of components D1–D4, and G can be found in a work by Sadezky et al. [65] and references therein. D1, D2 and D4 bands

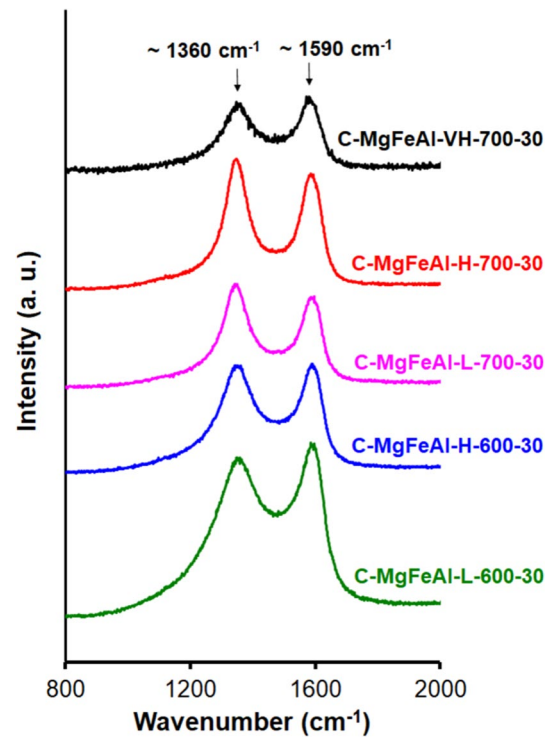


Figure 2 The Raman spectra of the carbon materials synthesized at 600 and 700 °C via CCVD/CVD in the presence of the compounds generated in situ from MgFeAl-L HTs, MgFeAl-H HTs and MgFeAl-VH HTs.

correspond to disordered graphitic lattice, while D3 band originates from amorphous carbon. In particular, D1 band is attributed to graphitic layer edges, whereas D2 band is attributed to graphitic layer surfaces (i.e. graphitic layers, which are not sandwiched between two other graphitic layers). D4 band is attributed to sp²–sp³ bonds or C–C and C=C stretching vibrations of polyene-like structures. G band corresponds to an ideal graphitic lattice. The numbers denoted I_{D1}, I_{D2},

Table 3 The area ratios of various components (D1, D2, D3, D4 and G) of the Raman spectra of the carbon materials prepared at 600 and 700 °C via CCVD/CVD (30 min) with the compounds derived from MgFeAl-L HTs, MgFeAl-H HTs and MgFeAl-VH HTs

Sample	$I_{D1}/I_G+I_{D1}+I_{D2}$	I_{D1}/I_G	I_{D2}/I_G	I_{D3}/I_G
C-MgFeAl-L-600-30	0.66	3.49	0.79	0.85
C-MgFeAl-L-700-30	0.63	2.37	0.37	0.44
C-MgFeAl-H-600-30	0.65	2.72	0.48	0.61
C-MgFeAl-H-700-30	0.61	2.19	0.41	0.35
C-MgFeAl-VH-700-30	0.62	2.19	0.34	0.40

I_{D3} , I_{D4} , and I_G are areas of the respective components (D1-D4 and G) obtained during the nonlinear fitting procedure. The numbers are used for the calculation of the parameters: $I_{D1}/(I_G + I_{D1} + I_{D2})$ (indicates degree of organization of carbonaceous material) and I_{D1}/I_G (proportional to the fraction of edge plane surfaces), I_{D3}/I_G (proportional to the fraction of amorphous carbon) or I_{D2}/I_G (inversely proportional to the thickness of graphitic domains). The $I_{D1}/(I_G + I_{D1} + I_{D2})$ ratio follows this order: C-MgFeAl-H-700-30 (0.61) < C-MgFeAl-VH-700-30 (0.62) < C-MgFeAl-L-700-30 (0.63) < C-MgFeAl-H-600-30 (0.65) < C-MgFeAl-L-600+30 (0.66).

SEM micrographs indicate that the carbon materials synthesized at 600 °C (Fig. 3a and b) exhibit similar morphologies, consisting primarily of aggregates of plate-like carbon particles. In contrast, the samples obtained at 700 °C (Fig. 3c–e) contain not only platelet-shaped carbon particles but also tubular carbon structures. HR-TEM micrographs further confirm that the carbon deposits consist of assemblies of graphitic layers (Fig. S6a and b), and the elongated carbon particles are hollow (Fig. S6c–d). Based on the SEM images, it appears that CNTs population in these materials differs. CNTs predominantly expose basal planes, whereas the plate-like carbon particles mainly expose edge planes. Raman spectroscopy shows that the ratio of edge planes to basal planes (I_{D1}/I_G) decreases with increasing carbonization temperature, with values of I_{D1}/I_G dropping from 3.49 or 2.72 for the samples synthesized at 600 °C to 2.37 or 2.19 for those synthesized at 700 °C (Table 3). This suggests that the contribution of tubular carbon particles increases as the carbonization temperature rises.

The increasing population of CNTs is accompanied by a decrease in nitrogen concentration, with values

of 10.0 or 5.1 wt% for the samples prepared at 600 °C, compared to 2.1–3.4 wt% for the samples synthesized at 700 °C, as determined by EA (Table 2). We can conclude that the degree of N-doping in the carbon materials is influenced by their morphology, which is governed by the synthesis temperature and the composition of the compounds present during the CCVD/CVD processes.

XPS measurements were conducted to identify the nitrogen functionalities incorporated into the N-doped carbon materials. Figure S7 displays the N/C atomic ratios determined by XPS, which will be discussed further. The application of a lower pyrolysis temperature, specifically 600 °C, promotes the incorporation of nitrogen (N/C ~ 0.088 and 0.048) into the graphitic structure of carbon particles, resulting in an increased number of structural defects ($I_{D1}/(I_G + I_{D1} + I_{D2}) \sim 0.66$ and 0.65). These samples, predominantly composed of platelet-shaped carbon particles, are characterized by relatively thin graphitic domains ($I_{D2}/I_G \sim 0.79$ and 0.48). In contrast, the samples prepared at 700 °C, which contain both plate-like carbon particles and CNTs (C-MgFeAl-L-700-30 and C-MgFeAl-H-700-30), exhibit thicker graphitic domains ($I_{D2}/I_G \sim 0.37$ and 0.41) compared to those prepared at 600 °C (C-MgFeAl-L-600-30 and C-MgFeAl-H-600-30). Furthermore, the carbon materials synthesized at 700 °C contain less amorphous carbon ($I_{D3}/I_G \sim 0.44$ and 0.35) than their counterparts prepared at 600 °C ($I_{D3}/I_G \sim 0.85$ and 0.61). This demonstrates that the synthesis conditions, such as temperature and the type of HTs, influence both the thickness of the graphitic domains and the contribution of amorphous carbon.

XPS analysis of the surface of the carbon materials reveals that the elemental carbon concentration ranges from 81.7 to 92.7 wt% (Table 4). Figure 4a and b shows high-resolution C 1 s spectra for C-MgFeAl-L-600-30, C-MgFeAl-L-700-30, C-MgFeAl-H-600-30, and C-MgFeAl-H-700-30. The core-level C 1 s spectra can be well fitted with six components. The most dominant component, located at a binding energy around 285 eV, is attributed to C–C and C–H bonds in sp^2 -hybridized graphitic carbon. The contribution of this component to the total C 1 s peak area is 37.3, 44.9, 48.9, 49.5 and 47.1% for C-MgFeAl-L-600-30, C-MgFeAl-L-700-30, C-MgFeAl-H-600-30, C-MgFeAl-H-700-30 and C-MgFeAl-VH-700-30, respectively. Based on the surface carbon concentration (at.%), we calculated the carbon concentration in graphite-like units, which are 32.1, 41.9, 44.4, 47.3 and 42.5% for

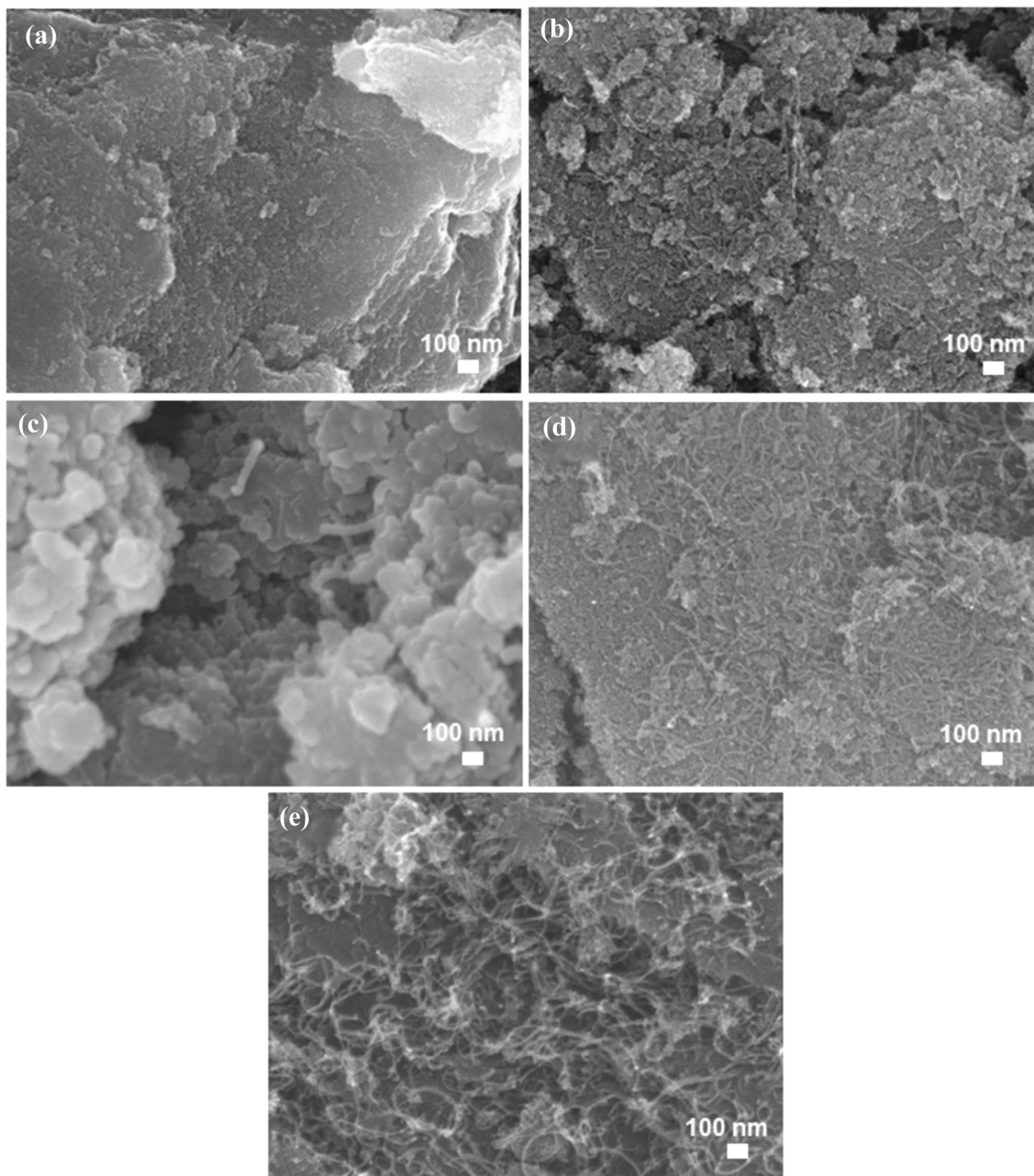


Figure 3 SEM micrographs of the carbon materials: C-MgFeAl-L-600-30 (a), C-MgFeAl-H-600-30 (b), C-MgFeAl-L-700-30 (c), C-MgFeAl-H-700-30 (d) and C-MgFeAl-VH-700-30 (e).

C-MgFeAl-L-600-30, C-MgFeAl-L-700-30, C-MgFeAl-H-600-30, C-MgFeAl-H-700-30 and C-MgFeAl-VH-700-30, respectively. Approximately 30–50%

of the surface carbon detected by XPS is attributed to carbon in a graphite-like structure. Furthermore, observed increase in sp^2 -hybridized graphitic carbon

Table 4 Surface (derived from XPS analysis) chemical composition of the carbon materials prepared at 600 and 700 °C via CCVD/CVD (30 min) with the compounds derived from MgFeAl-L HTs, MgFeAl-H HTs and MgFeAl-VH HTs

Sample	XPS analysis (wt%)							
	C	N	O	Mg	Fe	Al	Cl	N/C*
C-MgFeAl-L-600-30	81.7	8.3	6.8	–	1.4	–	1.8	0.088
C-MgFeAl-L-700-30	90.4	3.1	4.0	–	1.4	–	1.1	0.030
C-MgFeAl-H-600-30	86.6	4.9	4.4	0.6	1.7	0.2	1.6	0.048
C-MgFeAl-H-700-30	92.7	2.2	1.9	0.5	1.4	0.2	1.1	0.021
C-MgFeAl-VH-700-30	81.8	3.0	1.5	5.3	3.2	–	5.2	0.032

*Atomic ratio

indicates higher graphitization and consequently may be responsible for higher electrical conductivity.

Figure 4c and d present the N 1s core-level spectra for C-MgFeAl-L-600-30, C-MgFeAl-L-700-30, C-MgFeAl-H-600-30 and C-MgFeAl-H-700-30. The N 1s spectra can be deconvoluted into four distinct components, which are attributed to pyridinic N (at ~399 eV), pyrrolic N (at ~400–401 eV), graphitic N (at ~404–405 eV), and oxidized N (at ~407–408 eV) [66]. It is likely that nitrogen doping in the carbon materials predominantly occurs at the edges, as evidenced by the significant proportion of N-containing functional groups located at the graphite edge, including pyrrolic N (at pentagonal sites) and pyridinic N (at hexagonal sites). The percentages of these edge-bound N groups are 60.0, 60.2, 75.4, 77.0, and 89.2% for C-MgFeAl-H-700-30, C-MgFeAl-VH-700-30, C-MgFeAl-L-700-30, C-MgFeAl-H-600-30, and C-MgFeAl-L-600-30, respectively. Additionally, the contribution of graphitic N, which may also be present near the edge, ranges from 9.8 to 37.4%. Thus, the carbon materials are primarily characterized by N-containing groups located in edge-plane orientations of the graphitic structure. These findings align with previous literature, which suggests that N incorporation tends to favor non-planar environments, particularly at the edges, such as in pentagonal positions within hexagonally arranged carbon atoms [67, 68].

A closer examination of the N 1s spectra reveals that the relative contributions of pyrrolic N and pyridinic N decrease as the carbonization temperature increases, while the contribution of quaternary N increases (Fig. S8). A similar trend is reported for N-doped carbon materials derived from polyaniline (PANI) treated at different temperatures (800–1200 °C) [2], consistent with prior information indicating that the distribution of nitrogen functional groups shifts

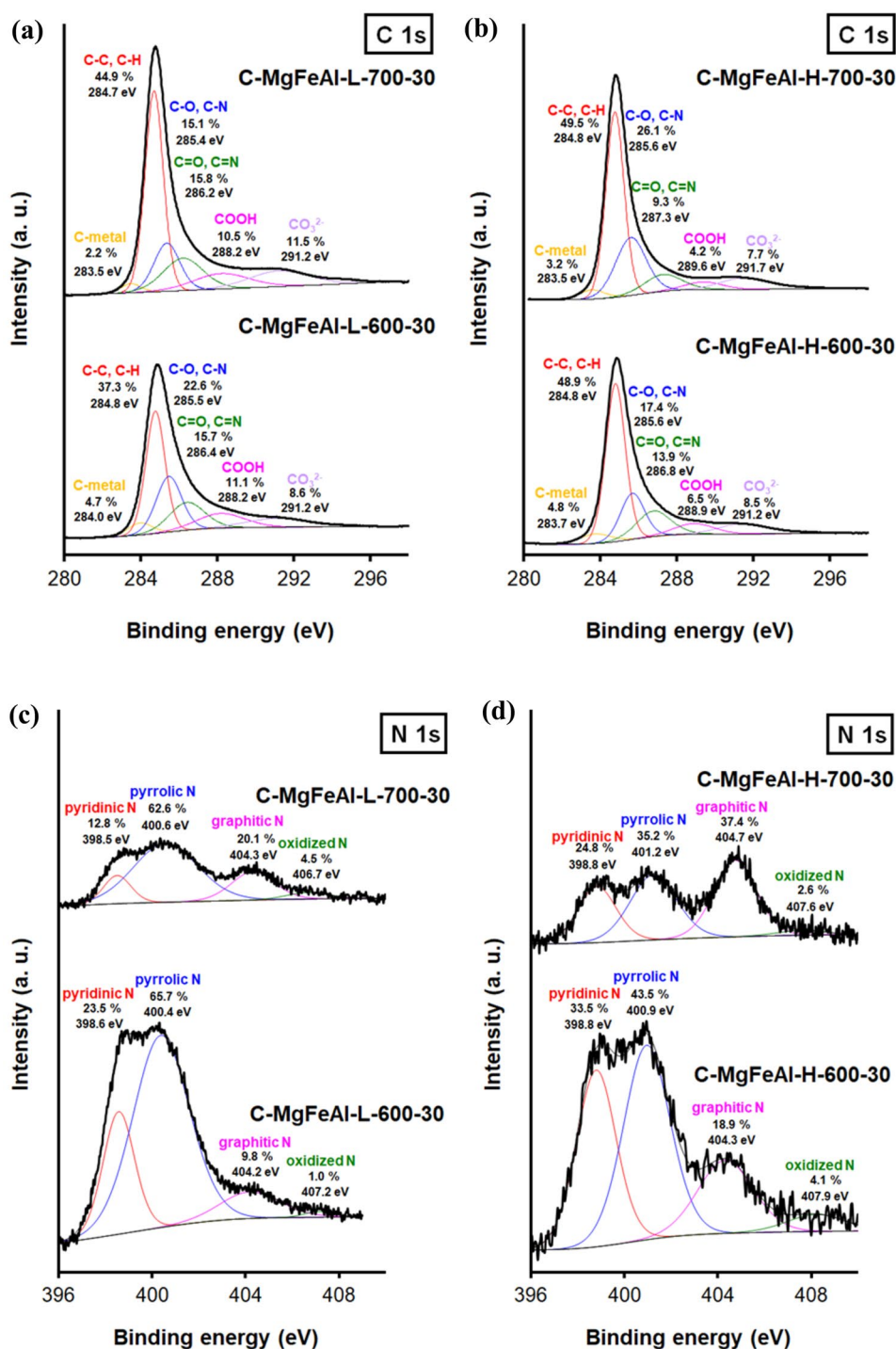
with more severe pyrolysis conditions [12, 69]. This shift is a result of the condensation process, where nitrogen atoms are incorporated into graphitic layers, replacing carbon atoms.

The bulk nitrogen content (2.1–5.1 wt%) measured by EA (Table 2) is very similar to the surface nitrogen content (2.2–4.9 wt%) determined by XPS (Table 4) for the studied carbon materials. The molar N/C ratios obtained by both techniques (EA vs. XPS) are also comparable (0.020 vs. 0.021, 0.027 vs. 0.030, 0.033 vs. 0.032, 0.052 vs. 0.048), further supporting the conclusion that nitrogen is uniformly distributed within the graphitic lattice.

XPS measurements also indicate that small amounts of magnesium (0.5–5.3 wt%) and aluminum (approximately 0.2 wt%) remain in the carbon materials prepared with MgFeAl-H HTs after acid treatment. These species are likely to be associated with traces of Mg–Al spinel remaining in the carbon materials following the acid treatment of the composites. Additionally, the presence of chlorine (1.1–5.2 wt%) in the carbon materials is confirmed by XPS. Chlorine species, such as Cl–C and Cl-metal, are likely to be formed during the treatment of the composites with HCl solution. A small amount of chlorine may remain in the samples after washing with the HCl solution, as reported elsewhere [18].

Figure 4e and f demonstrate that the carbon materials derived from MgFeAl HTs contain iron species, including both metallic Fe (Fe⁰) and oxidized forms (Fe²⁺ and Fe³⁺). Figures S9a and b, S10a and b further illustrate that iron species are well-distributed within the carbon materials. These species are present either as metallic Fe nanoparticles encapsulated in CNTs (Figs. S11a and b, S12a and b) or as partially oxidized metallic Fe nanoparticles intermixed with the carbon deposit. The surface concentration of iron,

Figure 4 The XPS spectra showing C 1s, N 1s, Fe 2p and O 1s signals for the carbon materials synthesized at 600 and 700 °C via CCVD/CVD in the presence of the compounds generated in situ from MgFeAl-L HTs, MgFeAl-H HTs and MgFeAl-VH HTs.

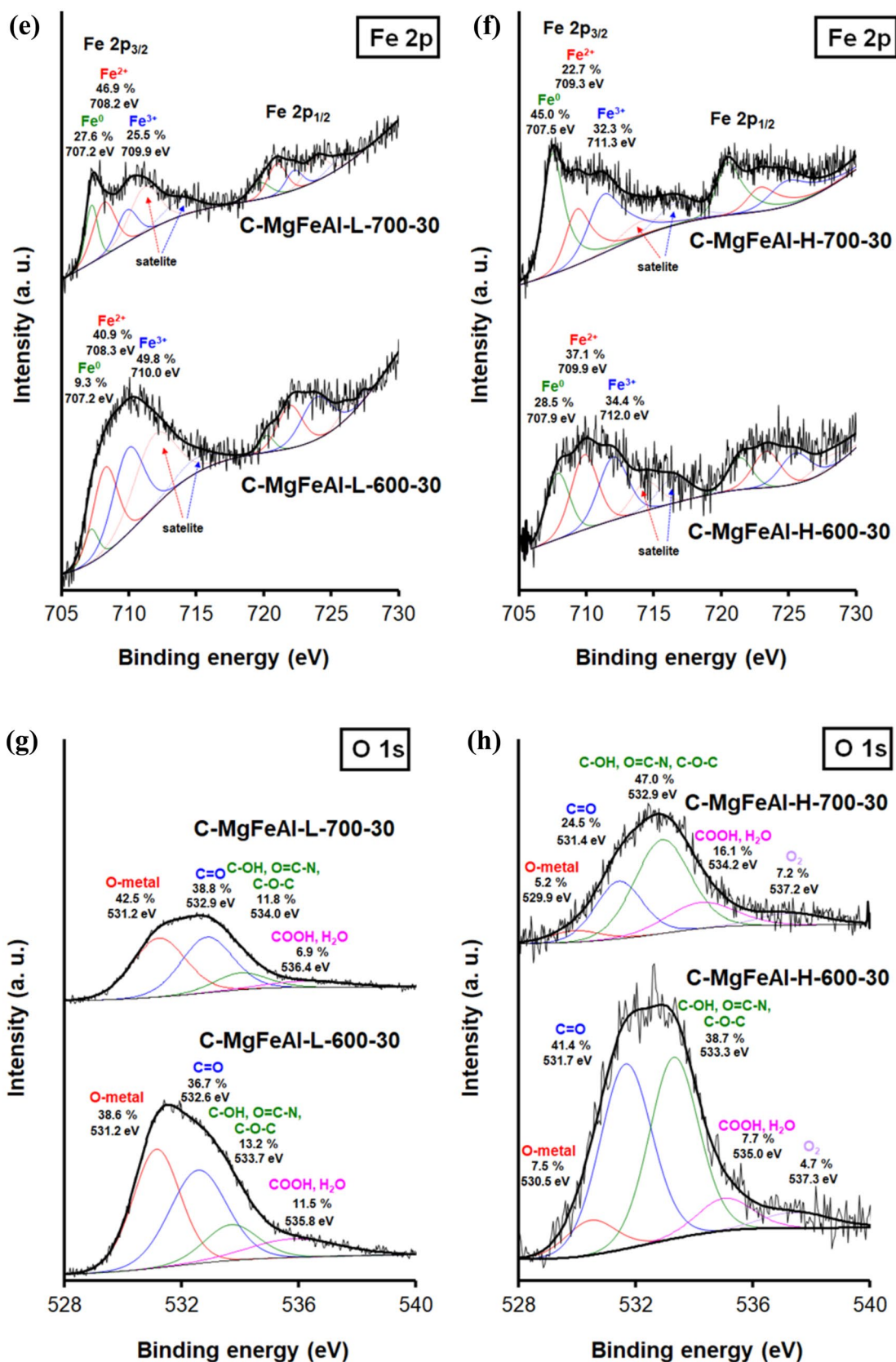


as determined by XPS, ranges from 1.4 to 3.2 wt% (Table 4), which is slightly lower than the bulk iron content (2.4–4.1 wt%) measured by XRF (Fig. S13a and b). XRF reveals that the bulk concentration of Fe depends on the concentration in the HTs, ranging from 2.4 to 2.6 wt% for the samples derived from MgFeAl-L

HTs, or 3.8–4.1 wt% for those from MgFeAl-H HTs. The bulk Fe concentration in C-MgFeAl-VH-700-30 is 2.4 wt%.

The presence of Fe-containing species on the surface of the carbon materials is further confirmed by cyclic voltammetry (CV) measurements. Previous

Figure 4 continued



studies report on the formation of $\text{Fe}(\text{OH})_2$ and Fe_3O_4 on iron surfaces exposed to alkaline solutions [70, 71]. The CV curves (Fig. S14) display small redox peaks corresponding to the reduction and oxidation of iron species in the carbon materials. However, in the case of the sample obtained at 600 °C with MgFeAl-L HTs, no such redox response is observed in the CV curve. We speculate that iron species may not be exposed to the electrolyte, either because they are completely shielded by a graphitic envelope or due to the current associated with the charging/discharging of the electrical double layer at the electrode/electrolyte interface, which may obscure the redox processes related to iron species. Faradaic processes related to iron species may be hidden by the large double layer charge as reported for Fe-N/AS and Fe-N/KUA immersed in N_2 -saturated aqueous solution (0.1 M KOH) [32]. A similar redox response due to the presence of Fe_3O_4 in the ORR electrocatalysts ($\text{Fe}_3\text{O}_4/\text{N-GAs}$, $\text{Fe}_3\text{O}_4/\text{N-GSs}$, $\text{Fe}_3\text{O}_4/\text{N-CB}$, $\text{Fe}_3\text{O}_4/\text{CN}_x\text{-Lys}$) was recorded in N_2 - and O_2 -saturated 0.1 M KOH [66, 72].

In addition, Mössbauer spectroscopy provides clear evidence of the presence of various iron species in the acid-treated samples derived from MgFeAl HTs (Fig. 5). The well-resolved low-temperature (193 °C) spectrum of C-MgFeAl-H-600-30 consists of five distinct components, corresponding to four sextets and one doublet (Fig. S15a). Among them, the components attributed to Fe_xO_y (non-stoichiometric FeO) and Fe_3C account for approximately 17 and 26%, respectively. Two additional components, attributed to Fe^{3+} -containing amorphous or defective phases, contribute 54% in total. The remaining 3% is ascribed to metallic iron (Fe^0). The fitted parameters are summarized in Table S1.

Similarly, the well-resolved low-temperature (193 °C) spectrum of C-MgFeAl-H-700-30 features three components: two sextets and one doublet (Fig. S15b and Table S2). The main component (48%) corresponds to Fe_3C . The second component, a doublet (37%), is attributed to iron atoms with threefold coordination by carbon and nitrogen in a nitrogen-defected Fe_3C structure. The ratio of the main component to the second component is 1.3: 1. The third component, contributing 15%, is assigned to Fe_xO_y .

The Mössbauer spectra of C-MgFeAl-L-600-30 and C-MgFeAl-H-600-30 recorded at room temperature exhibit similar features, suggesting the presence of analogous Fe-containing compounds in both carbon materials synthesized at 600 °C, despite the different

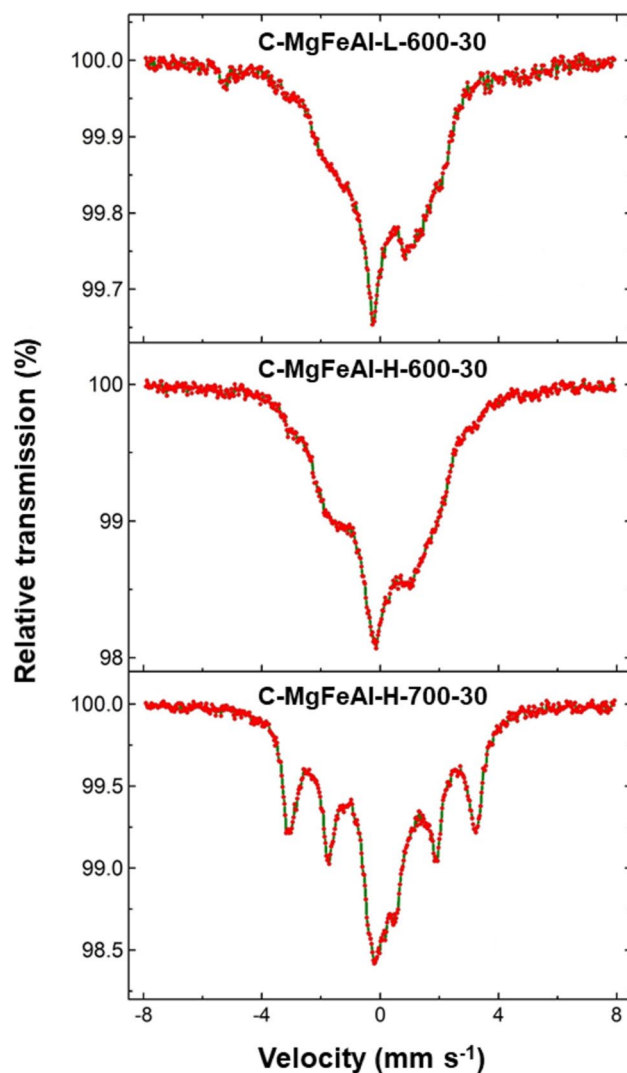


Figure 5 The Mössbauer spectra recorded at room temperature for the carbon materials denoted as C-MgFeAl-L-600-30, C-MgFeAl-H-600-30 and C-MgFeAl-H-700-30.

Fe content in the HTs used for their preparation. ^{57}Fe Mössbauer spectroscopy thus confirms the presence of diverse iron species in the acid-treated samples obtained with MgFeAl HTs exhibiting a broader variety of Fe-containing compounds in the samples prepared at 600 °C than in those prepared at 700 °C.

Having confirmed the presence of iron species on the surface of the studied materials, we cannot exclude the possibility that they may contribute to ORR, as they could be electrocatalytically active [32, 66, 72].

XPS studies confirm the presence of oxygen on the surface of the carbon materials. Figure 4g and h show high-resolution O 1s spectra for C-MgFeAl-L-600-30, C-MgFeAl-L-700-30, C-MgFeAl-H-600-30,

and C-MgFeAl-H-700-30. Four or five components are identified, corresponding to: (i) metal–oxygen bonds (at ~ 531 eV), (ii) C=O groups (at ~ 532 – 533 eV), (iii) C–OH, O=C–N, C–O–C bonds (at ~ 533 – 534 eV), and (iv) carboxyl groups (COOH), or adsorbed water (at ~ 534 – 536 eV) [73–75]. In addition, oxygen atoms in adsorbed O₂ molecules may contribute to the component at ca. 537 eV [76]. For the samples prepared with MgFeAl-L HTs, approximately 60% of the oxygen atoms are present on the surface of the graphitic lattice, while the remaining oxygen (around 40%) is likely in the form of inorganic compounds (e.g., MgAl₂O₄, iron species containing Fe²⁺ and Fe³⁺) that are covered by relatively thin carbon layers. In contrast, for the samples prepared with MgFeAl-H HTs, over 90% of the oxygen atoms are attached to the surface of the graphitic network, with the remaining oxygen (around 10%) associated with metal oxide species. The EDS analysis of HAADF micrographs, which show the distribution of four elements—carbon, nitrogen, oxygen, and iron—in the carbon materials (C-MgFeAl-H-700-30 and C-MgFeAl-VH-700-30), confirms the even distribution of C, N, O, and Fe within the samples (Fig. S9a and b, S10a and b).

The N₂ adsorption/desorption isotherms for the studied carbon materials, shown in Fig. S16a and b, display Type IV isotherms, characteristic of mesoporous materials [77]. Three distinct types of hysteresis loops—H2, H3, and H4—can be observed. Specifically, the H4-type loop for C-MgFeAl-L-600-30 suggests that this material consists of aggregates of plate-like particles with slit-shaped mesopores. The H2-type loops for C-MgFeAl-L-700-30, C-MgFeAl-H-600-30, and C-MgFeAl-H-700-30 indicate a more complex pore structure, consisting of aggregates of plate-like particles with slit-shaped mesopores of varying widths, such as bottleneck pores. The hysteresis loop with an H3-type profile for C-MgFeAl-VH-700-30 suggests that, in addition to mesopores within the plate-like particle aggregates, the sample also contains a pore network associated with macropores between CNTs.

The pore size distribution (PSD) profiles, presented in Fig. 6, reveal that the studied carbon materials besides mesopores contain also micropores. The ratio of micro- to mesopores ($V_{\text{micro}}/V_{\text{meso}}$) is 0.05, 0.09, 0.12, 0.14, and 0.15 (Table 5), demonstrating a clear predominance of mesopores in all the carbon samples. Notably, in the case of C-MgFeAl-VH-700-30, approximately 95% of the existing pores

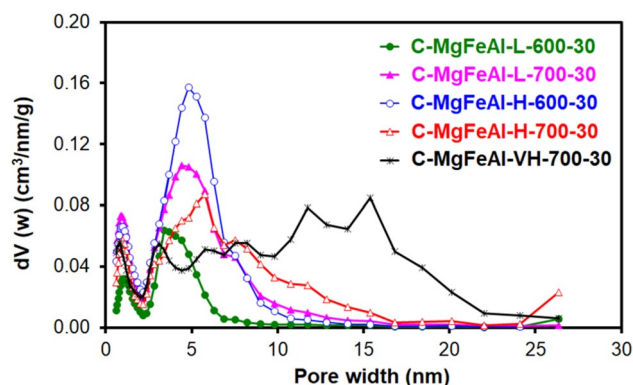


Figure 6 Micro/mesopore size distribution calculated using QSDFT method using N₂ adsorption/desorption data for the carbon materials synthesized at 600 and 700 °C, via CCVD/CVD in the presence of the compounds generated in situ MgFeAl-L HTs, MgFeAl-H HTs and MgFeAl-VH HTs.

are mesopores, resulting in a low $V_{\text{micro}}/V_{\text{meso}}$ value of 0.05, with only 5% of the total pore volume consisting of micropores. For the carbon materials prepared with MgFeAl-L HTs, mesopores account for 87–88%, while micropores make up 12–13%. The samples prepared with MgFeAl-H HTs exhibit comparable mesopore volumes (around 64%) but show the highest relative contribution of micropores (36%) among all the studied carbon materials. Figure 6 also illustrates that the choice of temperature and the chemical composition of HTs does not significantly impact the width of the micropores but they affect the diameter of the larger pores. The mesopore diameters for C-MgFeAl-L-600-30 are smaller (~ 2 – 7 nm) compared to those of the other carbon materials, where mesopore diameters range from ~ 2 to 13 nm for C-MgFeAl-L-700-30 and C-MgFeAl-H-600-30, and from ~ 2 to 17 nm for C-MgFeAl-H-700-30. Mesopore diameters for C-MgFeAl-VH-700-30 range from ~ 2 to 26 nm. This may result from the formation of a greater number of tubular carbon particles, which provide larger mesopores compared to plate-like carbon particles, which have mesopores with narrower diameters. Furthermore, the morphology of the carbon particles also influences the shape of the existing mesopores, as evidenced by the various hysteresis loops (H4→H2→H3).

Figure S17 demonstrates that the carbon materials derived from MgFeAl-L HTs exhibit lower pore volumes (0.227 and 0.584 cm³ g⁻¹, Table 5) compared to those obtained from MgFeAl-H HTs and MgFeAl-VH

Table 5 The textural properties (determined by N₂ adsorption) of the carbon materials prepared at 600 and 700 °C via CCVD/CVD (30 min) with the compounds derived from MgFeAl-L HTs, MgFeAl-H HTs and MgFeAl-VH HTs

Sample	Nitrogen sorption									
	S _{QSDFT} (m ² g ⁻¹)	V _{QSDFT} (cm ³ g ⁻¹)	V _{QSDFT} /S _{QSDFT} (nm)	S _{micro} (m ² g ⁻¹)	S _{meso} (m ² g ⁻¹)	V _{micro} (cm ³ g ⁻¹)	V _{meso} (cm ³ g ⁻¹)	V _{micro} /V _{meso}	V _{micro} /V _{QSDFT} × 100 (%)	V _{meso} /V _{QSDFT} × 100 (%)
C-MgFeAl-L-600-30	140	0.227	1.6	55	85	0.030	0.197	0.15	13	87
C-MgFeAl-L-700-30	342	0.584	1.7	146	196	0.072	0.512	0.14	12	88
C-MgFeAl-H-600-30	374	0.657	1.8	136	238	0.069	0.588	0.12	36	64
C-MgFeAl-H-700-30	287	0.659	2.3	103	184	0.053	0.606	0.09	36	64
C-MgFeAl-VH-700-30	337	1.056	3.1	115	222	0.054	1.002	0.05	5	95
Pt/C-MgFeAl-VH-700-30	318	0.902	2.8	105	213	0.043	0.859	0.05	5	95

The analogue results for Pt deposited on the carbon material labelled as C-MgFeAl-VH-700-30 are also included

HTs (0.657, 0.659, and 1.056 cm³ g⁻¹, Table 5), suggesting that a higher Fe content in Fe-containing HTs not only increases the amount of carbon deposit and influences total pore volume but also enlarges mesopores. The V_{QSDFT}/S_{QSDFT} ratio gradually increases from 1.6 and 1.7 nm for the carbon materials prepared with MgFeAl-L HTs to 1.8 and 2.3 nm for those prepared with MgFeAl-H HTs, and further to 3.1 nm for those obtained with MgFeAl-VH HTs (Table 5).

When comparing a pair of carbon materials derived from carbon deposits formed at 600 and 700 °C (9.8 and 26.3 wt%, respectively) using MgFeAl-L HTs, e.g. C-MgFeAl-L-600-30 and C-MgFeAl-L-700-30, we observe clear differences in their textural properties. The sample obtained at 700 °C exhibits significantly higher total pore volume (0.584 vs. 0.227 cm³ g⁻¹), mesopore volume (0.512 vs. 0.197 cm³ g⁻¹), and mesopore diameter (~ 2–13 nm vs. ~ 2–7 nm). In addition, the mesopore shape changes from an H4-type to an H2-type hysteresis loop, indicating a transition in pore structure.

A similar trend is observed in the carbon materials derived from carbon deposits formed at 600 and 700 °C (26.4 and 36.4 wt%, respectively) using MgFeAl-H HTs, e.g. C-MgFeAl-H-600-30 and C-MgFeAl-H-700-30. Although these samples display comparable total pore volumes (0.657 vs. 0.659 cm³ g⁻¹) and exhibit similar mesopore shapes (H2-type hysteresis), they differ slightly in mesopore volume (0.588 vs. 0.606 cm³ g⁻¹) and mesopore diameter (~ 2–13 nm vs. ~ 2–17 nm), both of which are greater in the sample obtained at 700 °C.

Further differences are evident when comparing another pair of carbon materials formed at 700 °C using MgFeAl-H HTs and MgFeAl-VH HTs (36.4 and 41.2 wt%, respectively), e.g. C-MgFeAl-H-700-30 and C-MgFeAl-VH-700-30. The latter shows significantly enhanced textural parameters, including total pore volume (1.056 vs. 0.659 cm³ g⁻¹), mesopore volume (1.002 vs. 0.606 cm³ g⁻¹), and mesopore diameter (~ 2–26 nm vs. ~ 2–17 nm). Additionally, a shift in mesopore shape is observed, from H2- to H3-type hysteresis, suggesting further modification in pore architecture.

We attribute the increased mesopore volume and diameter in these carbon materials to the partial removal of Fe from CNTs during acid washing. It is likely that the size of Fe NPs, which catalyse CNT growth, increases not only with higher carbonization

temperatures but also with higher Fe content in HTs. Based on this, we infer that the CNTs in C-MgFeAl-H-600-30 were formed with smaller Fe NPs than those in C-MgFeAl-H-700-30, while CNTs in C-MgFeAl-H-700-30 originated from smaller Fe NPs than those in C-MgFeAl-VH-700-30.

Electrocatalytic characterization of the carbon materials

The presence of structural imperfections and defects induced by nitrogen incorporation into the carbon framework plays a crucial role in the catalytic and electrocatalytic properties of N-doped carbon materials [78]. Carbon atoms adjacent to nitrogen atoms become active sites, facilitating processes such as the adsorption of oxygen molecule [1, 79]. Therefore, we aimed to investigate the potential of N-doped carbon materials as electrocatalysts for ORR, which can follow either a 2-electron or 4-electron pathway. Electrochemical behavior was evaluated using linear sweep voltammetry (LSV) measurements with a rotating disc electrode (RDE) made of glassy carbon (GC). Figure S18a–e show the LSV curves recorded for GC electrodes modified with the studied carbon materials, immersed in a 0.1 M KOH electrolyte saturated with oxygen. The plots reveal a two-step reaction mechanism for the carbon materials, suggesting a significant role for the 2-electron transfer process, leading to the formation of hydroperoxide anions (HO_2^-) as intermediates in alkaline electrolyte.

Figure 7a and b presents a comparison of polarization curves obtained at a rotation rate of 1600 rpm for GC electrodes modified with the carbon materials. The potential at the onset of the polarization curves allows for comparison of the ORR activity of the samples. The potentials corresponding to a current of -0.10 mA are as follows: -0.18 , -0.16 , -0.15 , -0.15 , and -0.13 V for C-MgFeAl-L-600-30, C-MgFeAl-H-600-30, C-MgFeAl-L-700-30, C-MgFeAl-H-700-30, and C-MgFeAl-VH-700-30, respectively. These values show an incremental improvement in ORR activity for the sample synthesized at 700 °C compared to those prepared at 600 °C. A similar increase in activity and selectivity towards ORR with increasing carbonization temperature (500, 600, and 700 °C) is reported for N-doped carbon materials derived from pyrrole [80].

Furthermore, the kinetic currents (obtained between -0.13 and -0.15 V) emphasize that the samples prepared at 700 °C are more active than those prepared

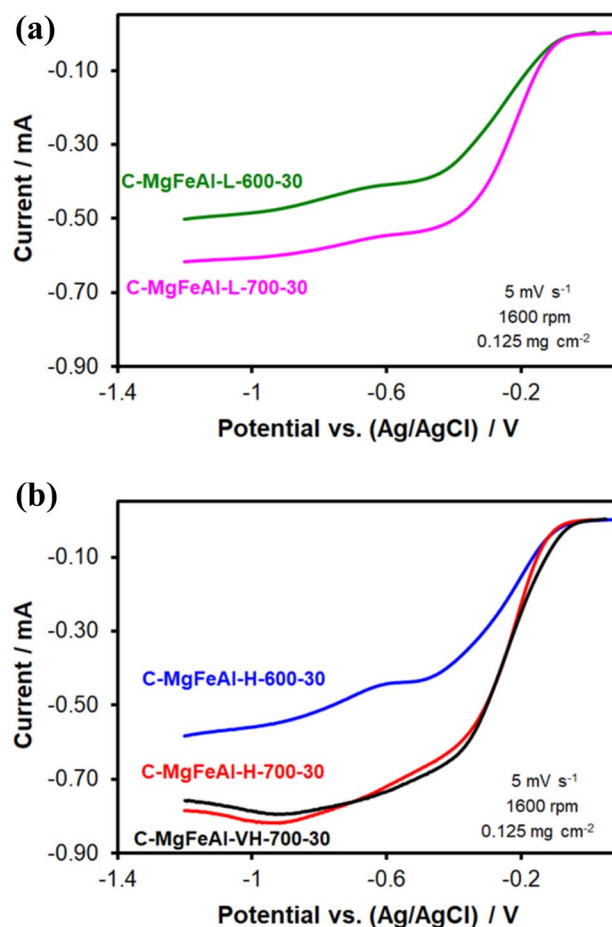


Figure 7 The comparison between current–potential relations recorded in the aqueous solution of O_2 -saturated 0.1 M KOH at 1600 rpm with a potential sweep rate of 5 mV s^{-1} for the carbon materials: C-MgFeAl-L-600-30 and C-MgFeAl-L-700-30 (a), C-MgFeAl-H-600-30, C-MgFeAl-H-700-30 and C-MgFeAl-VH-700-30 (b).

at 600 °C (Fig. S19a). Notably, C-MgFeAl-VH-700-30 exhibits the highest kinetic current among the studied materials. This may be attributed to a greater number of accessible active sites for oxygen in this sample, owing to its higher pore volume ($V_{\text{QSDFT}} = 1.056 \text{ cm}^3 \text{ g}^{-1}$), larger pore diameters (ranging from 2 to 26 nm), and the presence of macropores. Other studies also report on the positive influence of increasing mesopore diameters (22–50 nm) in mesoporous carbon spheres used as supports for Fe-based electrocatalysts, enhancing their ORR activity [81].

Figure 8a and b displays the Levich plots (i vs. $\omega^{1/2}$), which illustrate the relationship between the measured limiting current (at a potential of -0.9 V) and the square root of the rotation rate. The plots for the

Figure 8 The comparison between Levich plots for the oxygen reduction reaction over a GC coated with the carbon materials: C-MgFeAl-L-600-30 and C-MgFeAl-L-700-30 (a), C-MgFeAl-H-600-30, C-MgFeAl-H-700-30 and C-MgFeAl-VH-700-30 (b). The electron number was determined using the measured limiting currents at the potential of -0.9 V.

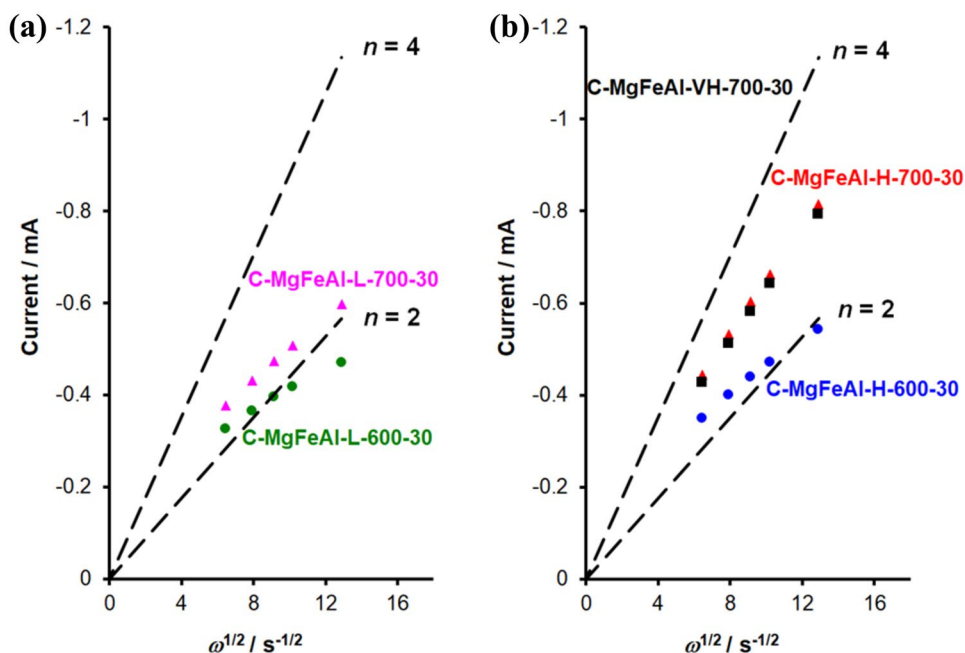


Table 6 The comparison of the data obtained from the electrochemical measurements in aqueous solution of O_2 -saturated 0.1 M KOH for the carbon materials prepared at 600 and 700 °C via CCVD/CVD (30 min) with the compounds derived from MgFeAl-L, MgFeAl-H and MgFeAl-VH HTs

Sample	Potential (V vs. Ag/AgCl)	Electron number	Tafel slope (mV dec ⁻¹)	
			Low current region	High current region
C-MgFeAl-L-600-30	-0.18	1.92	-111	-199
C-MgFeAl-H-600-30	-0.16	2.15	-114	-190
C-MgFeAl-L-700-30	-0.15	2.34	-97	-161
C-MgFeAl-H-700-30	-0.15	3.02	-90	-138
C-MgFeAl-VH-700-30	-0.13	2.93	-116	-202
Pt/C-MgFeAl-VH-700-30	-0.11	3.20	-94	-205
Pt/XC-72	-0.05	3.18	-90	-114

For comparison, the analogue results for Pt deposited on the carbon material labelled as C-MgFeAl-VH-700-30 (5 wt% Pt/C-MgFeAl-VH-700-30) and the commercial catalyst labelled as Pt/XC-72 (20 wt% Pt/C) are also included

samples prepared at 700 °C using MgFeAl-H HTs and MgFeAl-VH HTs lie between the theoretical lines for 2- and 4-electron reaction pathways. In contrast, the plots for C-MgFeAl-L-600-30, C-MgFeAl-H-600-30, and C-MgFeAl-L-700-30 align with the theoretical line for a 2-electron reaction.

The number of electrons involved in ORR (n) increases with higher synthesis temperatures and higher Fe content in the HTs, with values of 1.92, 2.15, 2.34, 2.93, and 3.02 (Table 6). Similar electron numbers ($n \sim 3$) for ORR in alkaline media, oscillating between 2 and 4, is reported for various N-doped carbon

materials [80, 82–84]. Furthermore, the presence of oxidized form of iron on the surface of the electrocatalysts (revealed by CV) during ORR may be responsible for mixed selectivity during ORR as previously reported for Fe/AS in alkaline solution [32]. The synthesis of the electrocatalysts with the application of CH_3CN vapor and MgFeAl HTs does not lead to more active and selective ORR catalysts than those already reported in the literature.

To assess the stability of the electrocatalysts, two samples, C-MgFeAl-L-700-30 and C-MgFeAl-H-700-30, were selected for continuous recording of 50

LSV curves in O₂-saturated 0.1 M KOH. The measurements were taken between the open circuit potential (~ 0 V) and -1.2 V at 1600 rpm, with a potential sweep rate of 5 mV s⁻¹, over a testing period of approximately 12,000 s. We conducted a similar evaluation for the commercial catalyst, 20 wt% Pt/C, and published the obtained data in our previous work [85]. The current results demonstrate that both the onset potential (Fig. S20a and b) and the number of electrons involved in ORR (Fig. S21a and b) remain stable. Furthermore, cyclic voltammograms (CV) recorded at a potential between the hydrogen and oxygen evolution reaction in the aqueous solution of O₂-saturated 0.1 M KOH for C-MgFeAl-L-700-30 and C-MgFeAl-H-700-30, before and after stability test are shown in Fig. S20c and d, additionally indicate the stability of these materials, with a weaker response to Faradaic process related to iron species as a result of iron dissolution. However, thorough surface characterization after prolonged operation is essential to confirm the long-term stability of the carbon-based electrocatalysts. Carbon materials undergoes degradation over time when subjected to an applied voltage in alkaline medium. Carbon oxidation to CO₂ and/or CO is a primary cause of corrosion, ultimately leading to the degradation of carbon-based electrodes. A range of techniques, such SEM coupled with EDX, XPS and Raman spectroscopy, can be employed to evaluate changes in the morphological and physicochemical properties of the carbon materials after extended use (e.g., during accelerated durability test, ADT).

Tafel analysis was performed (Fig. S22) using data from the polarization curves (Fig. S18a–f). The corresponding Tafel slopes for the low (-0.10 to -0.15 V) and high current regions (-0.15 to -0.25 V) are summarized in Table 6. The Tafel slopes for the carbon materials prepared at 700 °C, namely C-MgFeAl-L-700-30 and C-MgFeAl-H-700-30, are close to those for 20 wt% Pt/XC-72 (-90 and -114 mV dec⁻¹) [85]. In contrast, the Tafel slopes for the samples prepared at 600 °C, including C-MgFeAl-L-600-30 and C-MgFeAl-H-600-30, as well as C-MgFeAl-VH-700-30, are higher than those for the 700 °C samples. The reason for the Tafel slopes of C-MgFeAl-VH-700-30 being more similar to those of the 600 °C samples is not immediately clear. It may be due to a comparable number of active sites involved in ORR for both C-MgFeAl-VH-700-30 and the samples synthesized at 600 °C. Although the concentration of electrocatalytic sites in C-MgFeAl-L-600-30 seems to be higher than in

C-MgFeAl-VH-700-30, its lower pore volume and conductivity may limit its activity. In contrast, C-MgFeAl-VH-700-30, with fewer active sites, benefits from better oxygen access due to its larger pore volume and higher conductivity, facilitating 4-electron reduction over 2-electron reduction.

Electrochemical measurements confirm that C-MgFeAl-L-600-30 is the least active for ORR and the least selective for 4-electron reduction (Table 6). This sample has a high contribution of lamellar grains, exposing many edge plane sites ($I_{D1}/I_G = 3.49$) and a high nitrogen concentration (N/C = 0.088). However, access to electrocatalytic sites may be hindered by the small contribution of mesopores ($V_{\text{meso}} = 0.197 \text{ cm}^3 \text{ g}^{-1}$), leading to a relatively low number of accessible active sites. Additionally, the presence of thin graphitic domains ($I_{D2}/I_G = 0.79$) and a large amount of amorphous carbon ($I_{D3}/I_G = 0.85$) could contribute to its relatively low conductivity. Previous studies also demonstrate that development of electrical conductivity as well as surface area result in improved ORR activity [86, 87].

As the carbonization temperature increases and the Fe concentration in Fe-containing HTs rises, the total number of nitrogen atoms decreases (Fig. S7), and the defect population is reduced (Table 3). Despite this, the ORR activity of the studied samples improves, and the number of electrons involved in ORR increases, ranging between 2 and 4. The effects of the condensation reactions promoting the transformation of N-containing functional groups in the graphitic lattice, along with the increased formation of carbon nanostructures and higher Fe nanoparticle content are more pronounced at 700 °C. The specific N-containing functional groups (Fig. S8) and their distribution change, affecting the overall ORR performance.

According to the publication by Sharifi et al. [1], the condensation reaction induced by annealing N-doped carbon materials can convert existing N-containing functional groups, such as pyrrolic N, into N-Q_{valley} species and/or pyridinic N into both N-Q_{valley} and N-Q_{center} species. The ORR on nitrogen edge defects (e.g., pyrrolic-N, pyridinic-N, and N-Q_{valley} sites) proceeds predominantly through a 4-electron pathway. In contrast, the reaction follows a 2-electron pathway when occurring on bulk nitrogen defects, such as N-Q_{center} sites. Sharifi et al. also demonstrated that annealing at temperatures between 500 and 1000 °C leads to an increase in the total amount of quaternary N (N-Q), including both N-Q_{center} and N-Q_{valley}

species, with the increase being more pronounced for N- Q_{valley} . While our XPS measurements do not differentiate between N- Q_{valley} and N- Q_{center} , the observed electrochemical response indicates an increase in the number of electrons transferred with rising synthesis temperatures. This suggests that the contribution of N- Q_{valley} likely increases under these conditions.

Two samples obtained at 700 °C using HTs with either high or very high iron content can be classified as the most active and selective for 4-electron reduction among the studied carbon materials (Table 6). These samples contain relatively thick graphitic domains ($I_{D2}/I_G = 0.41$ and 0.34 , respectively) and minimal amounts of amorphous carbon ($I_{D3}/I_G = 0.35$ and 0.40 , respectively). As a result, their ability to transfer electron (conductivity) is expected to be superior to that of other samples, especially those prepared at 600 °C. C-MgFeAl-H-700-30 and C-MgFeAl-VH-700-30 exhibit a lower number of edge plane sites ($I_{D1}/I_G = 2.19$) (Table 3), likely due to the high population of CNTs, accompanied by relatively low N/C atomic ratios of 0.021 and 0.032, respectively (Table 4). When compared to C-MgFeAl-H-700-30, C-MgFeAl-VH-700-30 offers electrocatalytic sites responsible for higher kinetic current. This could be due to better access to the active sites in C-MgFeAl-VH-700-30, as it has a higher mesopore volume ($1.002 \text{ cm}^3 \text{ g}^{-1}$ vs. $0.606 \text{ cm}^3 \text{ g}^{-1}$) (Table 5) and a broader mesopore diameter range (2–26 nm vs. 2–17 nm).

Previous studies demonstrate that better electrical conductivity and higher mesopore surface area are critical for electron and mass transfer in fuel cell [88]. Judging by the contribution of sp^2 -hybridized graphitic carbon (determined by XPS), among both samples, C-MgFeAl-H-700-30 possesses better electrical conductivity than C-MgFeAl-VH-700-30. Although C-MgFeAl-H-700-30 is more conductive than C-MgFeAl-VH-700-30, its lower ORR activity may be attributed to other factors such as lower mesopore volume.

Both samples also have a higher proportion of quaternary N compared to the other studied samples, which may account for the increased number of electrons transferred (2.93 and 3.02 vs. 1.92, 2.15, 2.34). An increased selectivity for 4-electron O_2 reduction with a higher fraction of quaternary N is reported for N-doped carbon materials prepared at 500, 600, and 700 °C using pyrrole [80].

Our previous research on N-doped carbon materials obtained at 600, 700, and 800 °C using MgCoAl

HTs demonstrated that the increasing contribution of CNTs with carbonization temperature in a series of electrocatalysts (C-600, C-700, and C-800) could suppress their electrocatalytic performance [37]. However, in contrast to the previous results, the presence of CNTs in the current study appears to be beneficial for the ORR behavior of N-doped carbon materials obtained at 600 and 700 °C using Fe-containing HTs. According to the literature [89], the existence of CNTs in ORR electrocatalysts may be helpful as they are stable against corrosion during ORR and maintain high electrical conductivity.

According to the previous studies [90, 91], iron encapsulated in CNTs can positively impact ORR occurring on the surface of the CNTs. This effect is likely to be amplified by the incorporation of nitrogen atoms into the carbon framework. Indeed, iron is present inside the CNTs of the studied carbon materials (Figs. S11 and S12). The surface concentration of Fe, determined by XPS, is comparable across most of the studied samples, ranging from 1.4 to 1.7 wt% (Fig. S13a). Only C-MgFeAl-VH-700-30 has a higher surface Fe content (3.2 wt%).

A comparison of the binding energies for the Fe^0 component in the Fe 2p spectra (at 707.2 to 707.9 eV) and the C-metal component in the C 1s spectra (at 283.5–284.0 eV) reveals no shift in binding energy, suggesting no significant interaction between iron and the carbonaceous envelope. Furthermore, despite the nitrogen concentration and, more importantly, the contribution of nitrogen atoms located at the edges or near the edges—identified as key for ORR [1]—no clear correlation between activity/selectivity and the population of N-containing species could be established (Fig. S8).

Based on the observed potential values, the following order of ORR activity is seen: C-MgFeAl-L-600-30 < C-MgFeAl-H-600-30 < C-MgFeAl-L-700-30, C-MgFeAl-H-700-30 < C-MgFeAl-VH-700-30, which generally corresponds to the decreasing contribution of amorphous carbon ($I_{D3}/I_G = 0.85, 0.61, 0.44, 0.40, 0.35$) and the increasing thickness of the graphitic domains ($I_{D2}/I_G = 0.79, 0.48, 0.41, 0.37, 0.34$). Therefore, we hypothesize that electrical conductivity plays a significant role in the electrocatalytic performance of these materials, as previously emphasized by several studies [4, 66, 72, 86, 88]. However, the contribution of sp^2 -hybridized graphitic carbon (32.1, 44.4, 41.9, 47.3 and 42.5%) does not increase linearly across the samples ranked by catalytic activity,

indicating no straightforward correlation with electrical conductivity. This suggests that other factors, such as the nature and availability of active sites, mesopore volume, and pore diameter, play critical roles in determining performance.

We conclude that increasing synthesis temperatures from 600 to 700 °C enhances ORR activity, as evidenced by higher onset potentials and greater kinetic currents. Elevated temperature facilitates the formation of quaternary N, which increases selectivity for the 4-electron ORR pathway. Among the studied carbon materials, those prepared at 700 °C, i.e. C-MgFeAl-H-700-30 and C-MgFeAl-VH-700-30, demonstrated the best ORR performance, with C-MgFeAl-VH-700-30 exhibiting the highest kinetic current. This superior performance can be attributed to its larger pore volume, broader pore diameter range, and enhanced oxygen accessibility. Additionally, the presence of CNTs and thicker graphitic domains in the carbon materials synthesized at higher temperature may contribute to enhanced electron transfer and improved ORR activity. Furthermore, iron encapsulated within CNTs may positively impact on ORR activity.

Based on our experimental results, we propose that iron plays multiple roles in the system: (a) metallic iron formed during the CCVD process catalyzes the growth of carbon nanostructures; (b) acid washing removes not only Fe NPs that acted as catalysts but also other Fe-containing species partially embedded in the carbon matrix. This dissolution process creates pores, particularly when iron species are not fully encapsulated within CNTs or the carbon deposit. We attribute the observed increase in mesopore volume and diameter to the partial removal of Fe species during this treatment; (c) iron species (metallic or oxidized) exposed on the sample surface, and thus accessible to the electrolyte, may participate in ORR under applied voltage. This is supported by CV data and aligns with previous reports of mixed ORR pathways (both 2-electron and 4-electron) facilitated by such iron species, e.g. Fe₂O₃ [32, 66, 72]; (d) metallic iron encapsulated within carbon nanostructures, as revealed by electron microscopy, appears to have limited interaction with the surrounding carbon matrix (as indicated by XPS). Although not active in ORR, these encapsulated iron particles may improve the electrical conductivity of the carbon material, which is beneficial; (e) we found no evidence for the formation of nitrogen-coordinated Fe centres (Fe–N–C), which are typically associated

with high ORR activity. This observation is consistent with previous findings reported for Ozkan's catalysts.

We applied one of the studied carbon materials, namely C-MgFeAl-VH-700-30, as a support for Pt NPs. We decided to load a small amount of Pt (5 wt%) as other authors recommended [34, 36]. The presence of Pt crystallites in Pt/C-MgFeAl-VH-700-30 is confirmed by XRD (Fig. S23). Crystallite sizes for plane (111), (200) and (220) estimated by Scherrer equation are equal to 3.7, 5.5 and 12.1 nm, respectively. The contrast analysis of BSE images showing the distribution of four elements, i.e. carbon, oxygen, iron and platinum, confirms the presence of Pt evenly distributed on the grains of the carbon material (Fig. S24a and b). The BSE images reveal that besides Pt phase homogeneously distributed on the carbon material, it can also be perceived as the aggregates of Pt on C-MgFeAl-VH-700-30 indicated by a distinct bright spot.

Spreading Pt particles on C-MgFeAl-VH-700-30 does not affect the textural properties (Table 5) and pore size distribution of the support (Fig. S25), which suggests that Pt particles may reside on the outer surface of the support, between individual carbonaceous grains and/or aggregated Pt particles may locate on individual carbonaceous grains only partially block the entrance to the mesopores within carbonaceous grains.

The electrochemical measurements (Figs. S18f, S19b, S22, Table 6) reveal that Pt/C-MgFeAl-VH-700-30 is more active and more selective for 4-electron ORR than Pt-free C-MgFeAl-VH-700-30 as it contains additional active sites (Pt species). Even though the deposition of Pt onto C-MgFeAl-VH-700-30 leads to improved electrocatalytic properties, Pt/C-MgFeAl-VH-700-30 does not surpass the commercial Pt-based catalyst in terms of ORR activity.

Incorporation of the carbon materials into PCL-based composite films

Further investigations into the utilization of the carbon materials as components in the preparation of polymer-based composite films reveal that three samples—C-MgFeAl-L-700-30, C-MgFeAl-H-700-30, and C-MgFeAl-VH-700-30—differently influence the electrical and dielectric properties of PCL-based composite films.

PCL itself is an insulator, with the electrical conductivity of the pure PCL film measuring 2.88×10^{-10} S m⁻¹, a value consistent with previous reports [92].

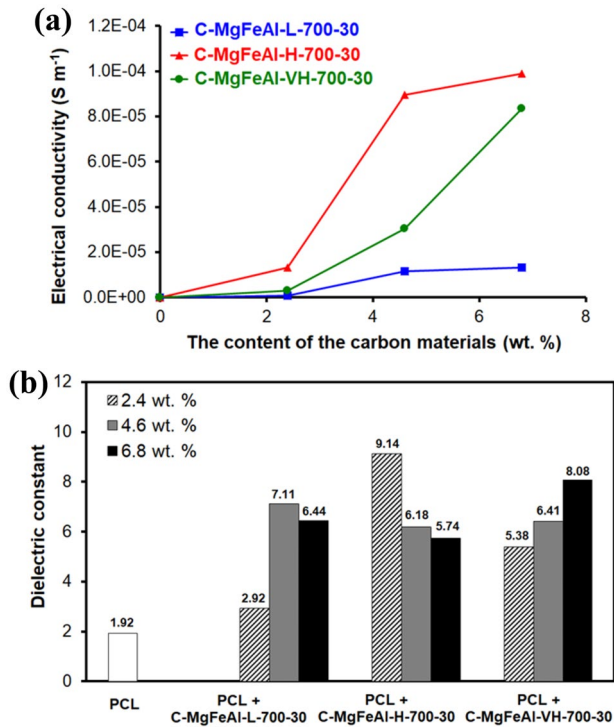


Figure 9 Dependence of the electrical conductivity (a) and the dielectric constant (b) of PCL-based composite films on the weight percentage (0, 2.4, 4.6 and 6.8 wt%) of the carbon materials (C-MgFeAl-L-700-30, C-MgFeAl-H-700-30, C-MgFeAl-VH-700-30).

Preliminary experiments focused on preparing PCL-based composite films with varying weight percentages of the carbon materials (2.4, 4.6, and 6.8%) reveal that the electrical conductivity of these composite films

increases with the amount of the carbon material incorporated. As shown in Fig. 9a and Table 7, the plot of AC conductivity versus carbon material concentration demonstrates that the percolation threshold occurs at a loading of approximately 2.4 wt% of the carbon material. Among the composite films, those prepared with C-MgFeAl-H-700-30 exhibit higher conductivity compared to those prepared with C-MgFeAl-L-700-30 or C-MgFeAl-VH-700-30. We assume that the electrical properties of the PCL-based composites may be associated with the degree of graphitization of the carbonaceous component and the presence of amorphous carbon in the studied carbon materials. According to the data achieved by Raman measurements (Table 3), the extent of defects in the carbon materials follows this order: C-MgFeAl-H-700-30 (0.61) < C-MgFeAl-VH-700-30 (0.62) < C-MgFeAl-L-700-30 (0.63), while the contribution of amorphous carbon follows the same order: C-MgFeAl-H-700-30 ($I_{D3}/I_G = 0.35$) < C-MgFeAl-VH-700-30 ($I_{D3}/I_G = 0.40$) < C-MgFeAl-L-700-30 ($I_{D3}/I_G = 0.44$). Furthermore, the contribution of graphitic carbon (determined by XPS) increases from 41.9 via 42.5 up to 47.3% for C-MgFeAl-L-700-30, C-MgFeAl-VH-700-30 and C-MgFeAl-H-700-30, respectively. Besides intrinsic features, also other properties such as the contribution of lamellar and tubular carbon particles plays a role. According to the literature [93–95], the morphology of the fillers in the composite materials affect their global electrical/dielectric response. Preliminary results demonstrate that the morphology of the carbon particles influences the distribution of the carbon component within the polymer matrix (Fig.

Table 7 The electrical conductivity (calculated from measured electrical resistance) of the composite membranes prepared with PCL and various amounts (2.4, 4.6 and 6.8 wt%) of the carbon

Sample	Carbon material (wt%)	Electrical conductivity (S m ⁻¹)	Carbon material (wt%)	Electrical conductivity (S m ⁻¹)	Carbon material (wt%)	Electrical conductivity (S m ⁻¹)
PCL+C-MgFeAl-L-700-30	2.4	$7.88 \pm 0.98 \times 10^{-7}$	4.6	$1.14 \pm 0.23 \times 10^{-5}$	6.8	$1.32 \pm 0.28 \times 10^{-5}$
PCL+C-MgFeAl-H-700-30	2.4	$1.31 \pm 0.36 \times 10^{-5}$	4.6	$8.96 \pm 0.61 \times 10^{-5}$	6.8	$9.89 \pm 0.35 \times 10^{-5}$
PCL+C-MgFeAl-VH-700-30	2.4	$3.00 \pm 0.63 \times 10^{-6}$	4.6	$3.04 \pm 0.37 \times 10^{-5}$	6.8	$8.35 \pm 0.91 \times 10^{-5}$
PCL+C-NiAl-H-600-30	2.4	$3.74 \pm 0.65 \times 10^{-5}$	4.6	$2.23 \pm 0.21 \times 10^{-4}$	6.8	$1.77 \pm 0.10 \times 10^{-4}$
PCL+C-NiAl-H-700-30	2.4	$1.80 \pm 0.63 \times 10^{-4}$	4.6	$4.19 \pm 0.48 \times 10^{-4}$	–	–
PCL+C-NiAl-H-800-30	2.4	$3.71 \pm 0.74 \times 10^{-4}$	4.6	$7.68 \pm 1.22 \times 10^{-4}$	–	–
PCL+C-NiAl-L-600-30	2.4	$1.03 \pm 0.13 \times 10^{-5}$	4.6	$1.45 \pm 0.63 \times 10^{-4}$	6.8	$1.90 \pm 0.59 \times 10^{-4}$
PCL+C-NiAl-L-700-30	2.4	$7.57 \pm 1.00 \times 10^{-5}$	4.6	$4.07 \pm 0.76 \times 10^{-4}$	–	–
PCL+C-NiAl-L-800-30	2.4	$1.65 \pm 0.53 \times 10^{-4}$	4.6	$6.47 \pm 1.7 \times 10^{-4}$	–	–

materials synthesized at 600, 700 and 800 °C using various HTs (MgFeAl-L, MgFeAl-H, MgFeAl-VH, NiAl-L and NiAl-H)

S26a–c, S27a–c, S28a–f). The carbon materials dominated by tubular carbon nanostructures seem to mix more effectively with the polymer compared to those primarily containing lamellar grains (Fig. S27a–c).

Figure S27a–c clearly illustrates that the carbon material in PCL-based composite films prepared with C-MgFeAl-L-700-30 is not evenly distributed, resulting in macroscopic aggregation of the carbon particles. Some aggregates are isolated by polymer coating preventing direct contact and thereby reducing conductivity. In contrast, both C-MgFeAl-H-700-30 and C-MgFeAl-VH-700-30, which contain a comparable proportion of plate-like particles to CNTs ($I_{D1}/I_G = 2.19$) and relatively more CNTs than C-MgFeAl-L-700-30 ($I_{D1}/I_G = 2.37$), therefore can be better blended with the polymer (Fig. S28a–f).

C-MgFeAl-L-700-30 shows macroscopic aggregation, whereas the carbon materials such as C-MgFeAl-H-700-30 and C-MgFeAl-VH-700-30 distribute more uniformly within the matrix. Despite certain similarities between C-MgFeAl-H-700-30 and C-MgFeAl-VH-700-30, the electrical properties of the corresponding composite films are different. We assume that metallic iron particles trapped in CNTs may contribute to the electrical conductivity of the composite films. XRF analysis reveals a higher iron content in C-MgFeAl-H-700-30 (4.1 wt%) compared to C-MgFeAl-L-700-30 (2.6 wt%) and C-MgFeAl-VH-700-30 (2.4 wt%). Thus, the electrical conductivity of the composite films may be influenced by the concentration, distribution, and chemical composition of iron species, which exist in both metallic and oxidized forms.

The difference between electrical conductivity of PCL+C-MgFeAl-H-700-30 and PCL+C-MgFeAl-VH-700-30 determined for the same carbon additive contents decreases with increasing quantity of the carbon material. It suggests that the formation a conductive network inside the polymer matrix by these two carbon materials develops in different ways, with a certain obstacle for C-MgFeAl-VH-700-30. The former may exhibit better compatibility with PCL than the latter or the studied carbon materials may contain the carbon particles with different dimensions. Indeed, other authors reported that spreading carbon additive in the polymer matrix depends on its particle size distribution [95] and on aspect ratio (length-to-diameter ratio) in the case of CNTs [96]. These are additional variables, which have to be taken into consideration. Perhaps not only a global distribution but also a local

dispersion of the carbon particles may play a role. We assume that C-MgFeAl-H-700-30 offers more charge carriers than C-MgFeAl-VH-700-30, which is a consequence of its composition (higher degree of graphitization, lower contribution of amorphous carbon) and higher content of metallic nanoparticles incorporated in CNTs. As a consequence, the highest conductivity ($\sigma = 9.89 \times 10^{-5} \text{ S m}^{-1}$) for PCL-based composite films is achieved for C-MgFeAl-H-700-30 at carbon additive concentration of 6.8 wt%.

SEM images (Fig. S29a and b) illustrate the presence of spherulites on the top and bottom surfaces of the pure PCL film, which are irregular in size and in shape. The PCL spherulites on the top surface have larger dimensions than those on the bottom surface probably because during crystallization process the top side of polymer solution being exposed to air had lower content of nucleation seeds (only internal one), whereas the bottom side of polymer solution being in contact with a glass surface (Petri dish) had a greater number of nucleation seeds (internal and external ones).

XRD patterns of PCL and PCL-based composite films (Fig. S30a–e) exhibit two broad reflections with peaks at $2\theta \sim 21.4^\circ$ and $\sim 23.7\text{--}23.8^\circ$, as well as a shoulder at $2\theta \sim 22.0\text{--}22.1^\circ$, corresponding to the (110), (200), and (111) diffraction planes of semi-crystalline PCL structure, respectively [97–101]. The intensity of the reflections characteristic of PCL gradually decreases in PCL-based composite films with increasing amount of the carbon materials, indicating a loss of crystallinity. This effect may be attributed to decreased concentration of PCL crystallites. Similar observations are reported for other PCL-based composites, i.e. containing various amounts of nanofibrillated chitosan (2.5, 5 and 10 wt%) [98] or grapefruit seed extract (GSE) (1, 3 and 5 wt%) [99] or graphene quantum dot (GQD) or a mixture (1:1) GQD and hydroxypropyl cellulose (HPC) [100]. In addition, the XRD data (Table S3) confirm a slight reduction in size of PCL crystallites with the presence of the carbon particles within the polymer matrix. The most pronounced effects are observed for PCL-based composites with the highest loading of the carbon materials (6.8 wt%), indicating high distribution and perhaps high dispersion of the carbon particles.

According to the literature [102], the addition of montmorillonite (MMT) (2.5, 4.6 and 8.1 wt%) to polypropylene (PP) in PP/MMT composites affected nucleation during crystallization of PP. The

Table 8 The dielectric constant (calculated from measured electrical capacitance) of the composite membranes prepared with PCL and various amounts (2.4, 4.6 and 6.8 wt%) of the carbon

materials synthesized at 600, 700 and 800 °C using various HTs (MgFeAl-L, MgFeAl-H, MgFeAl-VH, NiAl-L and NiAl-H)

Sample	Carbon material (wt%)	Dielectric constant	Carbon material (wt%)	Dielectric constant	Carbon material (wt%)	Dielectric constant
PCL+C-MgFeAl-L-700-30	2.4	2.92 ± 0.13	4.6	7.11 ± 0.18	6.8	6.44 ± 0.14
PCL+C-MgFeAl-H-700-30	2.4	9.14 ± 0.33	4.6	6.18 ± 0.10	6.8	5.74 ± 0.25
PCL+C-MgFeAl-VH-700-30	2.4	5.38 ± 0.44	4.6	6.41 ± 0.99	6.8	8.08 ± 0.40
PCL+C-NiAl-H-600-30	2.4	5.95 ± 0.79	4.6	6.61 ± 0.58	6.8	7.87 ± 0.62
PCL+C-NiAl-H-700-30	2.4	7.79 ± 2.11	4.6	5.01 ± 1.07	–	–
PCL+C-NiAl-H-800-30	2.4	8.84 ± 1.63	4.6	4.44 ± 0.84	–	–
PCL+C-NiAl-L-600-30	2.4	9.76 ± 0.65	4.6	9.11 ± 0.96	6.8	5.31 ± 0.61
PCL+C-NiAl-L-700-30	2.4	7.80 ± 0.97	4.6	3.94 ± 0.54	–	–
PCL+C-NiAl-L-800-30	2.4	8.78 ± 0.61	4.6	5.24 ± 0.12	–	–

crystallinity of PP in PP/MMT composites decreased with the increase in MMT content, indicating that the MMT layers dispersed in the PP matrices confined the PP chains and hindered the crystallization of the PP chains.

Based on the information prevailing in the literature, we assume that the carbon particles introduced into PCL solution constitute the nucleation centres, and consequently the growth of crystalline PCL in the studied PCL-based composites is suppressed by the presence of the carbon additive. Better blending of tubular carbon particles than plate-like carbon particles with PCL chains can more disturb PCL crystallization process. Indeed, significant changes in the surface morphology of PCL-based films are observed for PCL+C-MgFeAl-L-700-30 (SEM Fig. S31a–c) but especially for PCL+C-MgFeAl-VH-700-30 (Fig. S32a–c) compared to pure PCL. The authors reported that the spherulitic structure of PCL gradually disappeared for PCL-based composite containing 0.5 wt% CNTs or CNFs with the increasing number of the heterogenous nucleation seeds for the crystallization [46].

Figure 9b and Table 8 show the dielectric constants of PCL-based composite films as a function of carbon material loading. When a small amount (2.4 wt%) of carbon material is spread in the PCL matrix, numerous capacitors in the composites are formed, leading to an increase in dielectric constant ($\epsilon = 2.92, 5.38, 9.14$) compared to that of pure PCL ($\epsilon = 1.92$). The same quantity of various carbon materials leads to different dielectric properties as the contribution of lamellar and tubular carbon particles varies in each sample and therefore

the aggregates of the carbon materials in the polymer matrix occupy different volume fractions.

Even though digital images (Figs. S27a, S28a, d) illustrate that the carbon additive is more distributed in PCL+C-MgFeAl-VH-700-30 (2.4 wt%) than in PCL+C-MgFeAl-L-700-30 (2.4 wt%) and PCL+C-MgFeAl-H-700-30 (2.4 wt%), the highest value of dielectric constant ($\epsilon = 9.14$) is observed for PCL+C-MgFeAl-H-700-30 (2.4 wt%). It suggests that more interfaces are formed between the aggregates of C-MgFeAl-H-700-30 and the polymer matrix than in the case of other carbon materials, i.e. C-MgFeAl-L-700-30 and C-MgFeAl-VH-700-30. Knowing that the proportion of lamellar to tubular carbon particles is comparable for C-MgFeAl-H-700-30 and C-MgFeAl-VH-700-30, CNTs existing in both samples may differ in aspect ratio, which seems to be higher for the former compared to the latter.

As the carbon material content increases to 4.6 wt%, the dielectric constant rises progressively in the case of PCL-based composite films with C-MgFeAl-L-700-30 (2.92 → 7.11) and C-MgFeAl-VH-700-30 (5.38 → 6.41), whereas it decreases for the PCL-based composite film with C-MgFeAl-H-700-30 (9.14 → 6.18).

The distribution of the carbon additive in the volume of the matrix in PCL+C-MgFeAl-VH-700-30 (4.6 wt%) and PCL+C-MgFeAl-H-700-30 (4.6 wt%) may be comparable as seen with the naked eye (Fig. S27b, S28b, e). Moreover, these two composites have a similar value of dielectric constant (6.41 vs. 6.18), which suggests that the contribution of interfaces between the aggregates of either C-MgFeAl-VH-700-30 or

C-MgFeAl-H-700-30 and the PCL matrix may be also comparable. However, in the case of PCL+C-MgFeAl-H-700-30 (4.6 wt%) its dielectric properties are reduced compared to PCL+C-MgFeAl-H-700-30 (2.4 wt%). The value of ϵ decreases due to the formation of a conductive network and resultant leakage current within the composite, as observed in earlier studies [103]. According to the Fig. 9a, the conductivity of PCL+C-MgFeAl-H-700-30 (4.6 wt%) is distinctly higher than that of PCL+C-MgFeAl-VH-700-30 (4.6 wt%), therefore we assume that C-MgFeAl-H-700-30 compared to C-MgFeAl-VH-700-30 offers more charge carriers and/or it forms a more connected conductive network. It may be also associated with the presence of high-aspect-ratio CNTs in C-MgFeAl-H-700-30 compared to CNTs existing in C-MgFeAl-VH-700-30.

At a loading of 6.8 wt%, the dielectric constant increases only for PCL+MgFeAl-VH-700-30 system (6.41 \rightarrow 8.08), while it decreases for the others, such as PCL+C-MgFeAl-L-700-30 (7.11 \rightarrow 6.44) and PCL+C-MgFeAl-H-700-30 (6.18 \rightarrow 5.74). As seen with the naked eye (Figs. S27c, S28c and e), the carbon additive is only poorly distributed in PCL+C-MgFeAl-L-700-30 (6.8 wt%), whereas it is more uniformly blended with PCL in PCL+C-MgFeAl-H-700-30 (6.8 wt%) and PCL+C-MgFeAl-VH-700-30 (6.8 wt%). We assume that in the case of C-MgFeAl-VH-700-30, the carbon additive (6.8 wt%) is relatively highly distributed but its dispersion may be relatively poor, and the carbon particles still exist in small aggregates, which maintain the dielectric properties. In the case of other PCL-based composite films with high loading (6.8 wt%), the carbon material may be either highly distributed and highly dispersed in the case of C-MgFeAl-H-700-30 or poorly distributed and poorly dispersed in the case of C-MgFeAl-L-700-30.

The highest dielectric constant ($\epsilon = 9.14$) for PCL-based composite films is achieved for C-MgFeAl-H-700-30, which facilitates the highest number of interfaces between the carbon particles and PCL matrix even at relatively low carbon additive concentration, i.e. 2.4 wt%.

The quality and quantity of the carbon materials significantly affect the electrical and dielectric properties of the composite films (Tables 7 and 8). Features such as the degree of graphitization, the contribution of amorphous carbon, the content of metallic nanoparticles encapsulated in CNTs, the morphology of carbon grains (aggregates of plate-like particles, tubular nanostructures), non-uniform particle size

distribution, CNTs with different aspect ratios, and consequently volume fraction & aggregation effect are decisive factors. To support preliminary observations and our assumptions, we proceeded to prepare a new set of the composite films with the carbon materials characterized by varying contributions of CNTs and different nickel contents. These carbon materials were synthesized at temperatures of 600, 700, and 800 °C using CH₃CN in the presence of the compounds derived from NiAl HTs with varying Ni/Al atomic ratios (2 or 3), denoted as low (L) and high (H). The synthesis of these carbon materials was described in a previous study [8]. The CCVD experiments were carried out for 30 min. Immediately after synthesis, the as-received samples, consisting of carbon deposits and metals/metal oxides, were treated with acid to remove the majority of inorganic compounds and extract the carbon component. According to elemental analysis (EA), the carbon content in the acid-treated samples ranges from 75 to 86 wt% (Table S4). XRD (Figs. S33a and b, S34a–c, S35a–c) and XPS (Table S5) analyses confirm that the inorganic compounds in the acid-treated samples include metallic nickel covered with nickel oxide, nickel-aluminum oxide, and alumina. The acid-treated samples primarily contain CNTs, which exhibit a spaghetti-like appearance (Fig. S36a and b). Raman spectroscopy reveals that the ratio of edge planes to basal planes (I_{D1}/I_G) in the carbon materials decreases with increasing carbonization temperature. Specifically, the I_{D1}/I_G values decrease from 2.29 or 2.65 for samples prepared at 600 °C to 1.65 or 1.64 for those prepared at 700 °C, and further to 1.32 or 1.18 for samples prepared at 800 °C (Table S6). This trend suggests that the proportion of CNTs increases with higher carbonization temperatures.

Initially, three composite films were fabricated using C-NiAl-H-600-30 at 2.4, 4.6, and 6.8 wt% of the carbon material. The film with the highest carbon content (6.8 wt%) exhibited lower electrical conductivity than the one prepared with 4.6 wt% (1.77×10^{-4} vs. 2.23×10^{-4} S m⁻¹). This result indicates that a higher carbon content caused issues with the suspension's density and the blending of the components, particularly the integration of the carbon material into the polymer matrix. To avoid difficulties with the non-quantitative transfer of the suspension, leading to material loss, we decided to continue the preparation of the composite films with 2.4 and 4.6 wt% of carbon material, which allowed for more consistent and reliable results.

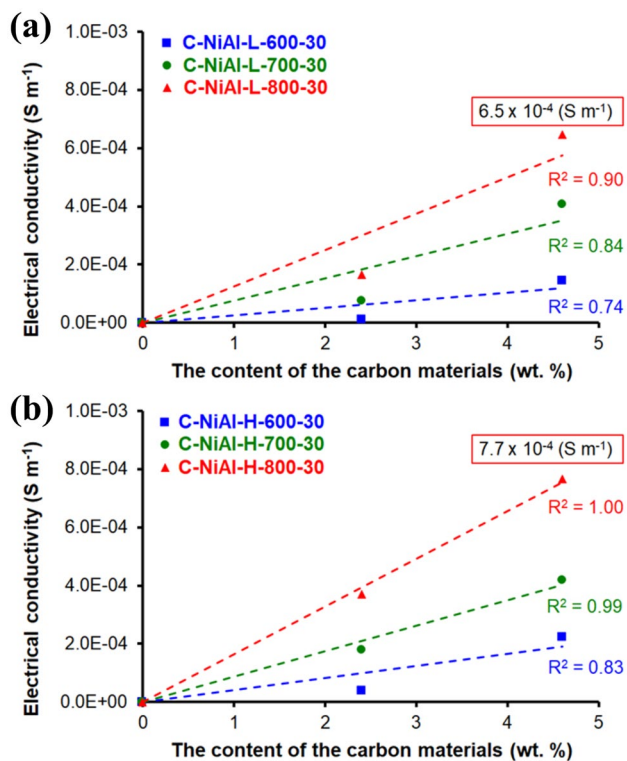


Figure 10 The linear dependence of the electrical conductivity of PCL-based composite films on the weight percentage (0, 2.4 and 4.6 wt%) of the carbon materials: C-NiAl-L-600-30, C-NiAl-L-700-30, C-NiAl-L-800-30 (a), C-NiAl-H-600-30, C-NiAl-H-700, C-NiAl-H-800 (b).

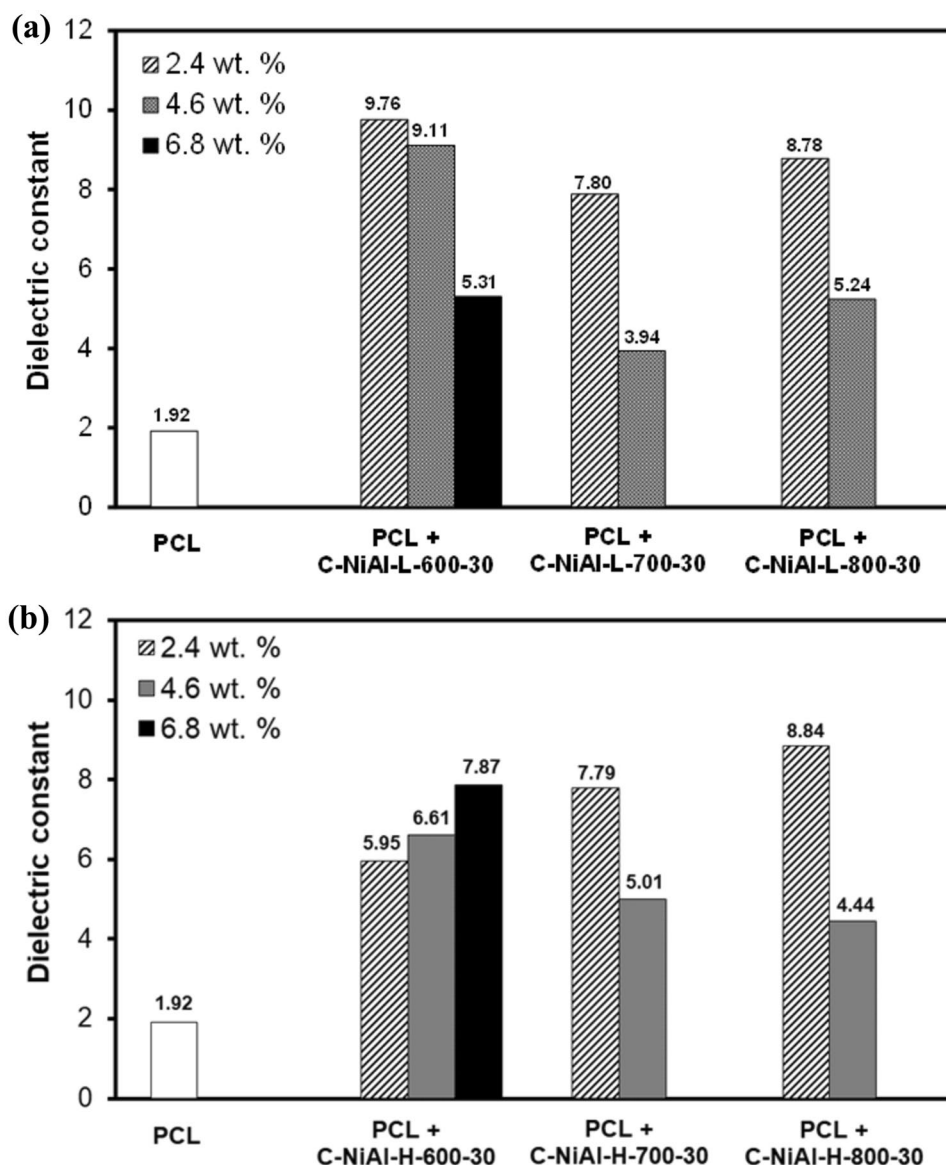
As shown in Fig. S37a and b and Table 7, the electrical conductivity of the composite films increases with the amount of the carbon material added as seen before for the composite films prepared with the carbon materials obtained with Fe-containing HTs. Moreover, Fig. 10a and b reveals a linear relationship between the conductivity of the composite films and the weight percentage of the carbon materials synthesized at 600, 700, and 800 °C. This indicates that conductivity increases with higher CCVD temperatures, likely due to the development of graphitic domains and the reduction of amorphous carbon contribution in the carbon component. Indeed, the contribution of sp^2 -hybridized graphitic carbon (determined by XPS) increases from 35.6 via 37.9 up to 41.5% for C-NiAl-H-600-30, C-NiAl-H-700-30 and C-NiAl-H-800-30, respectively. Note that the electrical conductivity of the composite films prepared with the carbon materials obtained with NiAl-L HTs (Fig. 10a) deviates more from a linear dependence on the carbon additive content than that of the composite films prepared with the

carbon materials obtained with NiAl-H HTs (Fig. 10b). This effect is especially pronounced for the composite films prepared with C-NiAl-L-600-30. Furthermore, it is also noticeable for the composite films prepared with C-NiAl-H-600-30. A slightly weaker correlation may be affected by the contribution of graphitic carbon (36.5, 41.8 and 36.4%, estimated by XPS), which does not increase linearly across the carbon materials obtained with NiAl-L HTs at increasing temperatures (600, 700 and 800 °C). Perhaps the intrinsic properties of the carbon materials (determined by Raman and XPS spectroscopy) play in some cases a less significant role in determining the electrical properties of the composite films.

Figure S38a–c shows that as the contribution of plate-like carbon particles decreases in the carbon materials obtained with NiAl-L HTs at higher CCVD temperatures, the composite films become less transparent, which is attributed to better distribution of carbon particles in the polymer matrix. The same trend is observed in Fig. S39a–c for the composite films prepared with the carbon materials obtained with NiAl-H HTs. The reduced population of lamellar grains in the carbon materials synthesized at 700 and 800 °C, coupled with a better distribution of the carbon particles in the PCL matrix, leads to the modification of the surface of the composite film with CNTs, as shown in the SEM images (Fig. S40a–d) for PCL-based composites containing 4.6 wt% of the carbon materials. Other authors also reported on SEM images illustrating the presence of tubular carbon nanostructures on the surface of PCL containing (5 wt%) highly dispersed MWCNTs [104].

The highest electrical conductivity, $7.68 \times 10^{-4} \text{ S m}^{-1}$, is achieved for the composite film prepared with the carbon material obtained at 800 °C with NiAl-H HTs. This material exhibits a high contribution of CNTs ($I_{D1}/I_G = 0.18$), a low contribution of amorphous carbon ($I_{D3}/I_G = 0.11$), and large graphitic domains ($I_{D2}/I_G = 0.15$). It is also possible that Ni nanoparticles encapsulated in CNTs contribute to the electrical conductivity of the composite film. The Ni content in C-NiAl-H-800-30 is 0.9 wt% (Table S5). However, upon closer inspection of the data (Table 7 and Table S5), no direct correlation can be found between the electrical conductivity of the composite films and the Ni concentration, as determined by XPS, in the corresponding carbon materials. The surface concentration of nickel decreases with increasing CCVD temperature, from 3.6 wt% at 600 °C to 1.9 wt% at 800 °C for the samples obtained with

Figure 11 The dielectric constant of PCL-based composite films as a function of the weight percentage (0, 2.4, 4.6 and 6.8 wt%) of the carbon materials: C-NiAl-L-600-30, C-NiAl-L-700-30, C-NiAl-L-800-30 (a), C-NiAl-H-600-30, C-NiAl-H-700, C-NiAl-H-800 (b).



NiAl-L HTs, and from 4.2 wt% at 600 °C to 0.9 wt% at 800 °C for the samples obtained with NiAl-H HTs, as shown in Fig. S41a. This trend contrasts with the observed effect of CCVD temperature on the electrical conductivity of the composite films. The bulk nickel concentration, measured by XRF (Fig. S41b), is higher than the surface nickel content determined by XPS, ranging from 3.6 to 8.0 wt% compared to the surface levels of 0.9 to 4.2 wt%. However, this does not suggest that the presence of nickel is a determining factor for the conductivity. It looks as the carbon component plays a more significant role in the electrical conductivity of the composite films than the presence of nickel species, due to its higher abundance.

The results presented in Fig. 11a and Table 8 demonstrate a four- to five-fold increase in the dielectric constant of pure PCL films after incorporating 2.4 wt% of the carbon materials synthesized at 600, 700, and 800 °C with NiAl-L HTs into the PCL matrix ($\epsilon = 9.76, 7.80, 8.78$). This shows that a small amount of each carbon material causes a more or less similar effect due to the formation of microcapacitor networks. Further increase in the loading of the carbon materials up to 4.6 wt% leads to a decrease in the dielectric constant values ($\epsilon = 9.76 \rightarrow 9.11, 7.80 \rightarrow 3.94, 8.78 \rightarrow 5.24$), likely due to higher distribution of carbon additive in the PCL matrix and the formation of a conductive network. No general trend is observed in the dielectric

constant values for the composite films prepared with the same carbon loading but using materials synthesized at different temperatures, even though Raman spectroscopy reveals variations in the proportion of lamellar to tubular grains with respect to CCVD temperature. Certainly other features of the carbon materials, apart from those revealed by Raman spectroscopy, have more significant influence on the global dielectric response of the composite films. Perhaps, CNTs in C-NiAl-L-600-30 may have higher aspect ratio than those in C-NiAl-L-700-30 and C-NiAl-L-800-30, and therefore the highest dielectric constant ($\epsilon = 9.76$) can be achieved for PCL-based composite film containing C-NiAl-L-600-30 at relatively low concentration, i.e. 2.4 wt%.

Figure 11b and Table 8 show the development of dielectric constants for the composite films prepared with the carbon materials obtained with NiAl-H HTs. A gradual increase in the dielectric constant is observed, rising from 5.95 to 7.79 to 8.84 for the films prepared with 2.4 wt% of the carbon materials synthesized at 600, 700, and 800 °C, respectively. The same amount of various carbon materials has different impacts on the dielectric properties of the composite films as they show varying proportion of grains with different morphology. Increase in the contribution of tubular nanostructures (as revealed by Raman), leads to increased degree of dispersion/distribution of the carbon grains, and consequently increased interfacial contact area between the carbon grains and the polymer matrix.

Further increase in the loading of the carbon materials up to 4.6 wt% leads to either an increase ($\epsilon = 5.85 \rightarrow 6.61$) or a decrease in the dielectric constant values ($\epsilon = 7.79 \rightarrow 5.01$, $8.84 \rightarrow 4.44$). Figures S38a–c and S39a–c illustrate that the distribution of the carbon materials prepared at 700 and 800 °C within the PCL matrix is higher than that for the carbon additive prepared at 600 °C. We assume that in the case of PCL+C-NiAl-H-700-30 (4.6 wt%) and PCL+C-NiAl-H-800-30 (4.6 wt%) their dielectric properties become suppressed probably due to the formation of more connected conductive network. On the other hand, the introduction of C-NiAl-H-600-30 (4.6 wt%) into the PCL matrix still allows to develop microcapacitance structures. Therefore we assume that CNTs in C-NiAl-H-600-30 may be characterized by lower aspect ratio than CNTs in C-NiAl-H-700-30 and C-NiAl-H-800-30.

Both C-NiAl-L-600-30 and C-NiAl-H-600-30 exhibit relatively high values of I_{D1}/I_G , 2.29 and 2.65,

respectively. These results suggest that the population of plate-like carbon particles may be slightly lower in C-NiAl-L-600-30 than in C-NiAl-H-600-30. Upon incorporating a small amount (2.4 wt%) of the carbon materials into the PCL matrix, the dielectric constant increases from 1.92 (for pure PCL film) to 9.76 for C-NiAl-L-600-30 and to 5.95 for C-NiAl-H-600-30. Further increasing the carbon content to 4.6 wt% leads to either a decrease in the dielectric constant ($9.76 \rightarrow 9.11$) for C-NiAl-L-600-30, or an increase ($5.95 \rightarrow 6.61$) for C-NiAl-H-600-30. These observations suggest that the proportion of tubular grains, which blend more easily with the polymer matrix than plate-like carbon materials, may be larger in C-NiAl-L-600-30 than in C-NiAl-H-600-30. To test this hypothesis, we prepared the composite films containing 6.8 wt% of C-NiAl-L-600-30 and C-NiAl-H-600-30, which show dielectric constants of 5.31 and 7.87, respectively, confirming that the carbon particles form a network of contacts in the former case. Figure S42a–c illustrate that the optical transparency of the composite films prepared with C-NiAl-L-600-30 gradually decreases and is eventually lost as the carbon content increases (2.4, 4.6, and 6.8 wt%). In contrast, Fig. S43a–c demonstrates that composite films prepared with C-NiAl-H-600-30 retain partial transparency across the entire range of carbon contents, showing the presence of a macroscopic network of black spots, indicative of a less uniform distribution of the carbon material in the polymer matrix. Thus, C-NiAl-L-600-30 containing more CNTs than C-NiAl-H-600-30 can be better distributed in PCL matrix. Furthermore, we assume that CNTs in the former may have higher aspect ratio than those in the latter. Therefore the highest dielectric constant ($\epsilon = 9.76$) for PCL-based composite films prepared with the carbon materials obtained with NiAl HTs is achieved for C-NiAl-L-600-30, which facilitates the highest population of interfaces between the carbon particles and the PCL matrix at relatively low carbon additive concentration, i.e. 2.4 wt%. This effect is similar to that observed for C-MgFeAl-H-700-30.

According to Rietveld analysis of the XRD patterns of the samples received just after CCVD experiments prepared with NiAl-L HTs at 600, 700 and 800 °C [8], the mean diameter of Ni crystallites is 9, 11 and 18 nm, respectively, whereas for those prepared with NiAl-H HTs at 600, 700 and 800 °C, the mean diameter of Ni crystallites is 14, 16 and 24 nm, respectively. The size of Ni crystallites increases with increasing Ni/Al atomic ratio and CCVD temperatures. The difference

between the values of Ni crystallite diameter for the samples prepared with NiAl-L HTs and NiAl-H HTs at the same temperatures (9 nm vs. 14 nm, 11 nm vs. 16 nm, 18 nm vs. 24 nm) is the most striking for the pair of samples prepared at 600 °C and decreases with increasing CCVD temperatures. These changes in the diameter of Ni crystallites existing in the as-received samples monitored by XRD could reflect in the size of Ni NPs being involved in the growth of CNTs. As the size of the catalyst (Ni) determines the diameter of CNTs, we may expect that the average diameter of CNTs increases not only with rising carbonization temperature but also with increasing Ni content in HTs. From this we can deduce that CNTs in C-NiAl-L-600-30 were formed with smaller Ni NPs than those in C-NiAl-H-600-30, therefore the former should have higher aspect ratio than the latter as they have smaller diameters. Similarly, CNTs in C-MgFeAl-H-700-30 probably were formed with smaller Fe NPs than those in C-MgFeAl-VH-700-30, for the same reason the former should have higher aspect ratio than the latter. Experimental data (dependence of dielectric constant values on carbon additive content in the composite films) are consistent with this assumption.

Extent of carbon additive distribution in the PCL-based composites has an influence on the contribution of crystalline PCL, as mentioned above for PCL-based composites prepared with the carbon materials synthesized with Fe-containing HTs. Figure S30d–e show XRD patterns recorded for two series of PCL-based films prepared with either C-NiAl-L-600-30 or C-NiAl-H-600-30 using various concentrations: 2.4, 4.6 and 6.8 wt% of carbon additive. The intensity of XRD reflection characteristic of semi-crystalline PCL is more suppressed by the introduction of C-NiAl-L-600-30 into PCL matrix than by C-NiAl-H-600-30. This observation is especially pronounced for the PCL-based composites with the highest concentration of the carbon material (6.8 wt%), which indicates distinct effects of high distribution/high dispersion of the carbon particles in the polymer matrix.

For composite films prepared with the carbon materials where the population of plate-like carbon particles is comparable ($I_{D1}/I_G = 1.65$ for C-NiAl-L-700-30 and $I_{D1}/I_G = 1.64$ for C-NiAl-H-700-30), the dielectric constants are nearly identical, with values of 7.80 and 7.79 for 2.4 wt% loading, and 3.94 and 5.01 for 4.6 wt% loading, respectively. A similar trend is observed for the composite films prepared with C-NiAl-L-800-30 and C-NiAl-H-800-30 ($I_{D1}/I_G = 1.32$

and 1.18, respectively), showing dielectric constants of 8.78 and 8.84 for 2.4 wt% loading, and 5.24 and 4.44 for 4.6 wt% loading. These results clearly indicate that the proportion of lamellar to tubular carbon grains in the carbon materials synthesized at the same temperature (700 or 800 °C) but using different NiAl HTs (L or H) is similar. Furthermore, CNTs in both carbon materials may have similar aspect ratios.

Metal contaminants in CNTs can increase toxicity by inducing cell death through mitochondrial damage and oxidative stress [105]. Given the presence of residual metals in the carbon materials, it is crucial to conduct appropriate biocompatibility tests, to ensure that PCL-based composite films are safe for short-term and non-invasive contact with human tissues. Additionally, these composites could be employed in contact-based, indirect applications, where electrical conductivity is beneficial but tissue exposure remains controllable. For instance, a layer of PCL/CNTs composite could serve as the electroactive component in flexible electronics in biomedical applications. The studied PCL-based composites exhibit a relatively low dielectric constant (< 10), which limits their suitability in some physical sensors, which require materials with a high dielectric constant [106].

Next, we examined whether the presence of CNTs near the surface of the composite film affects the surface properties of the PCL-based composite films or not. The water contact angle (WCA) for the top and bottom sides of the pure PCL film is $88.6 \pm 4.5^\circ$ and $82.0 \pm 4.1^\circ$, respectively, indicating the hydrophilic nature of the polymer ($WCA < 90^\circ$). Figure S44a–c, S45a and b, and S46a and b show the contact angles for both surfaces (top and bottom) of the composite films as a function of the carbon material content. For a small amount of carbon material (2.4 wt%), the contact angle for the top side ranges from 81.7 to 94.4° , and for the bottom side from 66.9 to 83.1° (Table S7). For a larger amount (4.6 wt%), the contact angle for the top surface is between 80.1 and 90.3° , and for the bottom surface between 67.5 and 80.4° (Table S7). The hydrophilic properties of the PCL-based composite films are largely retained, as the films are predominantly composed of polymer. Furthermore, FT-IR spectra recorded for the composite films for both sides: top (Figs. S47a, S48a) and bottom (Figs. S47b, S48b), show only spectroscopic response characteristic of PCL [107] because PCL is the major component, whereas the carbon additive exists on the surface in small quantities. It demonstrates that the population

of the carbon particles on both surfaces is insignificant. Thus the surface properties of the composite films are dominated by the polymer characteristics. However, the carbon additive itself has a potential for reducing the water contact angle as the carbon materials contain functional groups (O-, N-, Cl-containing). Such an impact is reported for MWCNTs/polysulfone (PSf) blend films [108]. Other authors [109], explained the reduction in WCA measured for MWCNTs/PCL composites by the presence of oxygen-containing species, such as hydroxyl and carboxylic groups, on the MWCNTs surface that protrude from the composite or by changes in surface roughness.

Experimental results indicates a slight enhancement of the hydrophilic properties on the bottom side of the composite film in comparison to the top one, which can be noticed even for pure PCL film. The possible explanation for such an observation is that the crystallization process of PCL may be affected by the contact of the polymer solution with the glass surface (Petri dish) being an additional source of nucleation seeds. As a result, the contributions of crystalline phase of PCL and its amorphous form on the surface of PCL-based film change depending on the side, which is also reflected in morphology (Fig. S29a and b) and topography (Fig. 12a and b). Furthermore, the introduction of the carbon additive enhances this effect as the carbon materials, especially tubular carbon nanostructures (which can be more easily blended with PCL than plate-like carbon particles) disturbs the crystallization process of PCL (as evidenced by XRD) leading to reduced population of PCL crystallites. This phenomenon is more likely on the bottom side of the composite films due to the sedimentation of the carbon material during film formation, enriching the bottom side with carbon additive relative to the top and influencing the proportion of crystalline PCL phase to its amorphous form. We assume that increasing amount of the carbon materials in the composite films is responsible for increasing exposure of amorphous PCL phase on both sides but especially on the bottom one.

Some authors report that pure PCL film can be characterized by WCA of $93 \pm 5^\circ$ and therefore it is considered to be hydrophobic as $WCA > 90^\circ$ [110]. Using such criterion, top surfaces of PCL+C-NiAl-L-700-30 (2.4 wt%) and PCL+C-NiAl-H-700-30 (2.4 wt%) show somewhat hydrophobic properties, but such results are only exceptions.

Figure 12a–f show three-dimensional (3D) AFM images of the top and bottom surfaces of pure PCL

and PCL-based composite films, along with the corresponding surface roughness (RMS) values. The 3D images reveal that the topography of the top surface of pure PCL films is varied, with extensive smooth areas with the RMS value of 182 nm, and boundaries between these flat regions, and larger voids resembling triangular holes (Fig. S49a and b). The bottom surface of the pure PCL film is smoother, with the RMS value of 44 nm, as confirmed by SEM images (Fig. S49c–d), indicating more uniformity due to the pressure exerted by the film's contact with the glass surface of the Petri dish during formation. Thus, the bottom surface of the PCL-based film can be deformed under compression. Furthermore, the PCL spherulites on the top surface have larger dimensions than those on the bottom probably because during PCL crystallization process, polymer exposed to the air has less nucleation seeds (only internal) than PCL exposed to the glass (both internal and external).

The addition of a small amount of carbon material (2.4 wt%) does not significantly alter the topographical properties of the film, as RMS values remain similar. However, SEM images (Fig. S50a–d) show that a small addition of the carbon material affects the morphology of the top surface, making it less diverse and reducing the size and contribution of the holes. With a higher carbon material content (4.6 wt%), the topographical features of both surfaces change, as RMS values decrease for the top surface and increase for the bottom. As a result, the difference between the two surfaces becomes smaller (88 nm vs. 140 nm). SEM images (Fig. S51a–d) show that the topography of both surfaces becomes more similar with the addition of the carbon material. It happens like that as the carbon additive (C-NiAl-H-800-30) disturbs crystallization process of PCL and as a consequence a lower number of PCL crystallites is formed as evidenced by XRD (Fig. S52a). A similar decrease in the intensity of XRD reflections characteristic of PCL after blending PCL with the carbon material can be seen for the analogue set of films prepared with C-NiAl-L-800-30 (Fig. S52b).

Both SEM and AFM microscopy techniques confirm that the surface morphology and topography are modified by the incorporation of additives in varying ratios. The changes in the water contact angle and RMS values—top: 182 nm → 187 nm → 88 nm; bottom: 44 nm → 68 nm → 140 nm—suggest that the film's hydrophilic properties are influenced not only by the chemical composition of the surface of the film but also by its topographical properties.

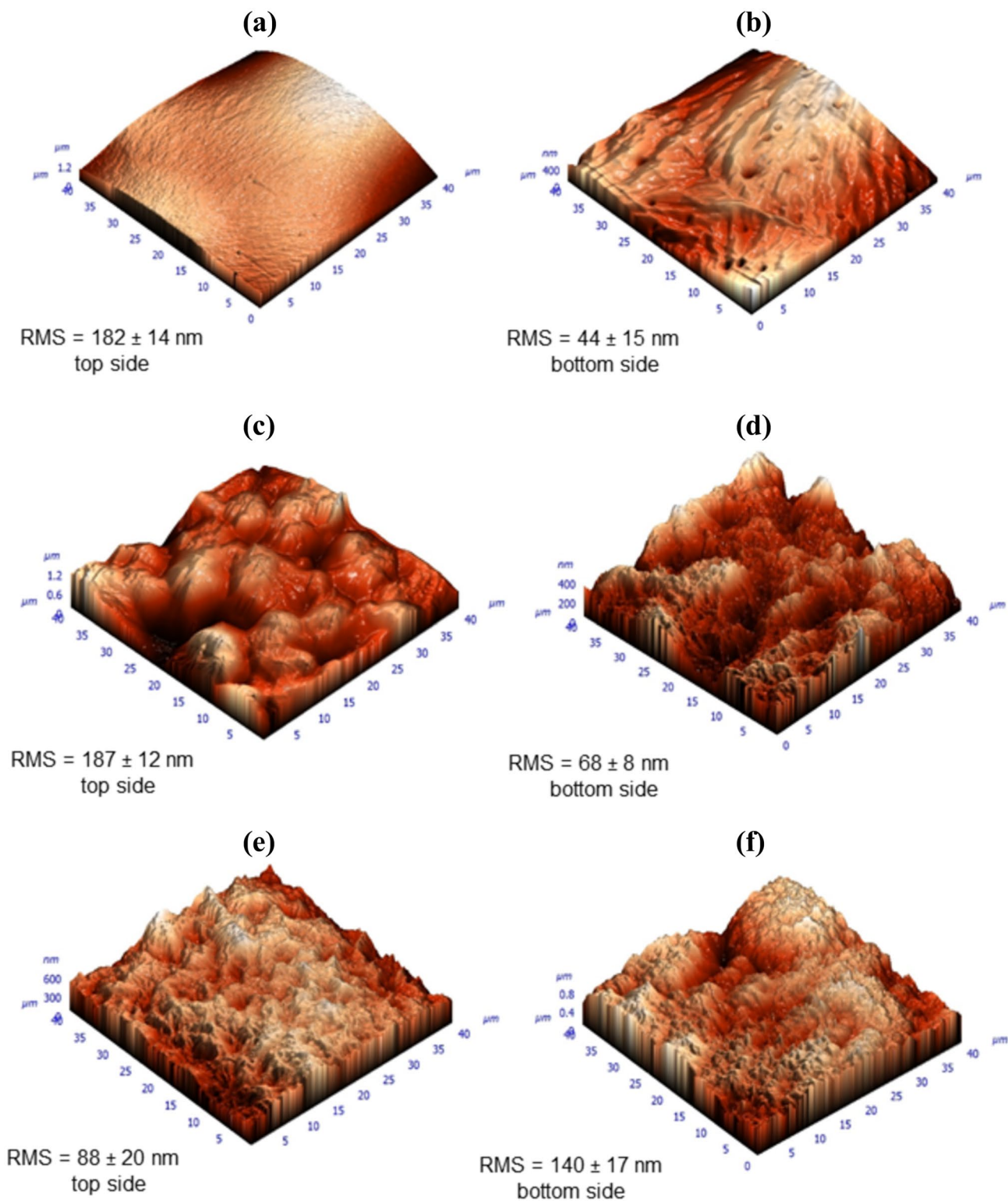


Figure 12 3D images from ($40 \times 40 \mu\text{m}$) $1600 \mu\text{m}^2$ scanning areas and root mean square (RMS) (nm) values by AFM for top and bottom sides of pure PCL film (a and b), PCL+C-NiAl-H-800-30 (2.4 wt%) (c–d) and PCL+C-NiAl-H-800-30 (4.6 wt%) (e–f).

The presence of CNTs on the surface of the PCL-based composite films is evidenced by SEM only in some cases. Furthermore, the population of carbon additive on the surface of the PCL-based composite films is scarcely, so the carbon materials cannot be detected by FT-IR. It implies that the carbon particles have minimal direct effects on the hydrophilic nature of the PCL-based films. Increasing loading of the carbon materials, especially increasing distribution of the carbon additive, reduces voids formation and morphological diversity of both sides, which leads to more uniform roughness across both sides of the films. Our observations are consistent with previous studies demonstrating that MWCNTs, acting as numerous crystallization nuclei, significantly disturbed the process of spherulite growth, what in a consequence, led to obtain more uniform and compact surface morphology [111]. It seems that the carbon materials via impact on PCL crystallization and consequently the proportion of crystalline to amorphous PCL phases, are responsible for slight reductions in water contact angles, especially on the bottom side of the films, where sedimentation enriches carbon particle distribution and emphasizes their influence on the growth of PCL crystallites.

Conclusions

Our findings underscore the critical role of synthesis conditions, particularly temperature (600 °C, 700 °C) and Fe concentration in MgFeAl HTs, in determining the pore structure and the incorporation of N- and Fe-containing species in the carbon materials derived from acetonitrile. These factors are instrumental in enhancing the ORR performance of N-doped carbon materials in alkaline environment.

Electrochemical measurements demonstrate that the synthesized N-doped carbon materials exhibit strong potential for hydrogen peroxide (H_2O_2) production, a key process in advanced water purification technologies based on the electrochemical degradation of contaminants. Additionally, carbon materials co-doped with nitrogen and iron—where iron is introduced via dissolution in alkaline solution—can promote Fenton-like reaction. In this process, Fe^{2+} reacts with H_2O_2 to generate hydroxyl radicals ($\cdot\text{OH}$) and hydroxide ions (OH^-), which subsequently degrade organic pollutants present in wastewater.

Furthermore, the results demonstrate how synthesis parameters, including temperature and Fe or Ni content in HTs, influence the structural and morphological characteristics of the carbon materials, thereby affecting the electrical and dielectric properties of PCL-based composite films. These insights establish a valuable framework for improving composite film performance by selecting the carbon materials with tailored properties and achieving precise control over their incorporation into the polymer matrix. Although the conductivity of the composite films does not reach the highest values reported in the literature, PCL reinforced with CNTs demonstrates satisfactory electrical conductivity. However, its biomedical application is limited by potential cytotoxicity, primarily due to residual metal catalyst nanoparticles (e.g., Fe, Ni) commonly present in CNTs as synthesis by-products. These metal contaminants may negatively impact cell viability, especially in long-term or direct-contact applications. Metal impurities can be removed via purification combining heat and acid treatments, which would make the carbon materials less toxic but also less active for ORR. Instead of employing PCL-based composite films in internal scaffold applications, a more appropriate approach would be to utilize them in contact-based, indirect applications, where electrical conductivity is advantageous but tissue exposure is controllable. The combination of these two components enables the creation of a flexible, stretchable material that simultaneously exhibits the ability to conduct electrical signals.

Acknowledgements

This research received funding from National Centre for Research and Development (NCBiR, Poland), agreement number EIG CONCERT-JAPAN/1/2019. Electrochemical measurements were performed by means of the equipment purchased thanks to the financial support of National Science Centre (NCN, Poland), decision number DEC-2013/11/B/ST5/01417. Professor Paweł Nowak (Jerzy Haber Institute of Catalysis and Surface Chemistry, Polish Academy of Sciences) is gratefully acknowledged for fruitful discussions. Dr. Ewelina Jarek (Jerzy Haber Institute of Catalysis and Surface Chemistry, Polish Academy of Sciences) is gratefully acknowledged for operating guidelines before FT-IR measurements. This research paper is dedicated to the memory of Dr. Jan Żukrowski

(1947–2024)—a widely known and respected specialist in the field of Mössbauer spectroscopy, who died while this paper was being peer-reviewed.

Author contributions

AP: conception, experimental design, carrying out synthesis of the HTs, the composites, the carbon materials, the composite films, recording of XRD patterns, FT-IR spectra, CV and LSV curves, measuring resistance and capacitance, performing analysis and interpretation of the data obtained by various methods/techniques, manuscript composition, writing—correcting and editing, funding acquisition. JG: carrying out XPS measurements. RPS: carrying out XPS measurements. PP: carrying out measurements via Raman spectroscopy. MR-M: carrying out N₂ sorption measurements. DD: carrying out SEM measurements. MK: carrying out water contact angle measurements. MN-R: carrying out AFM measurements. GM: carrying out XRF measurements. JŻ: carrying out measurements via Mössbauer spectroscopy. M.S: synthesis and characterization of Pt NPs and deposition of Pt NPs on the selected carbon material. B.D.N: carrying out N₂ sorption measurements.

Data availability

Not applicable.

Declarations

Conflict of interest The authors declare that they have no known competing financial interests or personal relationships that could have appeared to influence the work reported in this paper.

Ethical approval Not applicable.

Supplementary Information The online version contains supplementary material available at <https://doi.org/10.1007/s10853-025-11081-4>.

Open Access This article is licensed under a Creative Commons Attribution 4.0 International License, which permits use, sharing, adaptation, distribution and reproduction in any medium or format, as long

as you give appropriate credit to the original author(s) and the source, provide a link to the Creative Commons licence, and indicate if changes were made. The images or other third party material in this article are included in the article's Creative Commons licence, unless indicated otherwise in a credit line to the material. If material is not included in the article's Creative Commons licence and your intended use is not permitted by statutory regulation or exceeds the permitted use, you will need to obtain permission directly from the copyright holder. To view a copy of this licence, visit <http://creativecommons.org/licenses/by/4.0/>.

References

- [1] Sharifi T, Hu G, Jia X, Wågberg T (2012) Formation of active sites for oxygen reduction reactions by transformation of nitrogen functionalities in nitrogen-doped carbon nanotubes. *ACS Nano* 6(10):8904–8912
- [2] Quílez-Bermejo J, Melle-Franco M, San-Fabián E, Morallón E, Cazorla-Amorós D (2019) Towards understanding the active sites for the ORR in N-doped carbon materials through fine-tuning of nitrogen functionalities: an experimental and computational approach. *J Mater Chem A* 7:24239–24250
- [3] Quílez-Bermejo J, Morallón E, Cazorla-Amorós D (2020) Metal-free heteroatom-doped carbon-based catalysts for ORR: a critical assessment about the role of heteroatoms. *Carbon* 165:434–454
- [4] Kong F, Cui X, Huang Y, Yao H, Chen Y, Tian H, Meng G, Chen C, Chang Z, Shi J (2022) N-doped carbon electrocatalysts: marked ORR activity in acidic media without the contribution from metal sites? *Angew Chem Int Ed* 61:e202116290–e202116300
- [5] Ooi PC, Xie M, Dee CF (2022) Enhanced carbon-based materials and their applications, 1st edn. Wiley-VCH
- [6] Pacuła A, Mokaya R (2007) Layered double hydroxides as templates for nanocasting porous N-doped graphitic carbons via chemical vapour deposition. *Micropor Mesopor Mater* 106:147–154
- [7] Pacuła A, Drelinkiewicz A, Ruggiero-Mikołajczyk M, Pietrzyk P, Socha RP, Krzan M, Nattich-Rak M, Duraczyńska D, Bielańska E, Zimowska M (2022) N-doped carbon materials produced by CVD with the compounds derived from LDHs. *J Mater Sci* 57:18298–18322
- [8] Pacuła A, Nowak P, Socha RP, Ruggiero-Mikołajczyk M, Mucha D, Bielańska E (2013) Preparation and characterization of the electroactive composites containing nickel nanoparticles and carbon nanotubes. *Electrochim Acta* 90:563–572
- [9] Pacuła A, Gurgul J, Micek-Ilnicka A, Pietrzyk P, Ruggiero-Mikołajczyk M, Napruszewska BD, Duraczyńska D, Cempura G (2024) Capacitors and catalyst supports based on pyrolytic carbon deposited on metals/metal oxides derived from hydro-talcite-like materials. *J Mater Sci* 59:2788–2813
- [10] Lalande G, Côté R, Guay D, Dodelet JP, Weng LT, Bertrand P (1997) Is nitrogen important in the formulation of Fe-based catalysts for oxygen reduction in solid polymer fuel cells. *Electrochim Acta* 42:1379–1388

- [11] Côté R, Guay D, Lalonde G, Dodelet JP, Dénès G (1998) Influence of N-containing precursors on the electrocatalytic activity of heat-treated Fe(OH)₂ on carbon black for O₂ reduction. *J Electrochem Soc* 145(7):2411–2418
- [12] Faubert G, Côté R, Guay D, Dodelet JP, Dénès G, Poleunis C, Bertrand P (1998) Activation and characterization of Fe-based catalysts for the reduction of oxygen in polymer electrolyte fuel cells. *Electrochim Acta* 43:1969–1984
- [13] Faubert G, Côté R, Dodelet JP, Lefèvre M, Bertrand P (1999) Oxygen reduction catalysts for polymer electrolyte fuel cells from the pyrolysis of Fe^{II} acetate adsorbed on 3,4,9,10-perylene-tetracarboxylic dianhydride. *Electrochim Acta* 44:2589–2603
- [14] Matter PH, Zhang L, Ozkan US (2006) The role of nanostructure in nitrogen-containing carbon catalysts for the oxygen reduction reaction. *J Catal* 239:83–96
- [15] Matter PH, Ozkan US (2006) Non-metal catalysts for dioxygen reduction in an acidic electrolyte. *Catal Lett* 109:115–123
- [16] Matter PH, Wang E, Arias M, Biddinger EJ, Ozkan US (2006) Oxygen reduction reaction catalysts prepared from acetonitrile pyrolysis over alumina-supported metal particles. *J Phys Chem B* 110:18374–18384
- [17] Matter PH, Wang E, Ozkan US (2006) Preparation of nanostructured nitrogen-containing carbon catalysts for the oxygen reduction reaction from SiO₂- and MgO-supported metal particles. *J Catal* 243:395–403
- [18] Matter PH, Wang E, Arias M, Biddinger EJ, Ozkan US (2007) Oxygen reduction activity and surface properties of nanostructured nitrogen-containing carbon. *J Mol Catal A: Chem* 264:73–81
- [19] Biddinger EJ, von Deak D, Ozkan US (2009) Nitrogen-containing carbon nanostructures as oxygen-reduction catalysts. *Top Catal* 52:1566–1574
- [20] Matter PH, Wang E, Millet J-MM, Ozkan US (2007) Characterization of the iron phase in CN_x-based oxygen reduction reaction catalysts. *J Phys Chem C* 111:1444–1450
- [21] Singh D, Soykal II, Tian J, von Deak D, King J, Miller JT, Ozkan US (2013) *In situ* characterization of the growth of CN_x carbon nano-structures as oxygen reduction reaction catalysts. *J Catal* 304:100–111
- [22] Singh D, Tian J, Mamtani K, King J, Miller JT, Ozkan US (2014) A comparison of N-containing carbon nanostructures (CN_x) and N-coordinated iron-carbon catalysts (FeNC) for the oxygen reduction reaction in acidic media. *J Catal* 317:30–43
- [23] Zhao Y, Jiao Q, Li C, Liang J (2007) Catalytic synthesis of carbon nanostructures using layered double hydroxides as catalyst precursors. *Carbon* 45:2159–2163
- [24] Cao Y, Zhao Y, Jiao Q (2010) Fe-based catalysts from Mg/Fe layered double hydroxides for preparation of N-doped carbon nanotubes. *Mater Chem Phys* 122:612–616
- [25] Zhao M-Q, Zhang Q, Zhang W, Huang J-Q, Zhang Y, Su DS, Wei F (2010) Embedded high density metal nanoparticles with extraordinary thermal stability derived from guest-host mediated layered double hydroxides. *J Am Chem Soc* 132:14739–14741
- [26] Zhao M-Q, Zhang Q, Huang J-Q, Nie J-Q, Wei F (2010) Layered double hydroxides as catalysts for the efficient growth of high quality single-walled carbon nanotubes in a fluidized bed reactor. *Carbon* 48:3260–3270
- [27] Tian G-L, Zhao M-Q, Zhang Q, Huang J-Q, Wei F (2012) Self-organization of nitrogen-doped carbon nanotubes into double-helix structures. *Carbon* 50:5323–5330
- [28] Zhao M-Q, Liu X-F, Zhang Q, Tian G-L, Huang J-Q, Zhu W, Wei F (2012) Graphene/single-walled carbon nanotube hybrids: one-step catalytic growth and applications for high-rate Li-S batteries. *ACS Nano* 6:10759–10769
- [29] Feng J, Cai R, Magliocca E, Luo H, Higgins L, Fumagalli Romario GL, Liang X, Pedersen A, Xu Z, Guo Z, Periasamy A, Brett D, Miller TS, Haigh SJ, Mishra B, Titirici M-M (2021) Iron, Nitrogen Co-doped carbon spheres as low cost, scalable electrocatalysts for the oxygen reduction reaction. *Adv Funct Mater* 31:2102974–2102983
- [30] Zhong X, Shao Y, Chen B, Li C, Sheng J, Xiao X, Xu B, Li J, Cheng H-M, Zhou G (2023) Rechargeable zinc-air batteries with an ultralarge discharge capacity per cycle and an ultralong cycle life. *Adv Mater* 35:2301952–2301961
- [31] Lilloja J, Mooste M, Kibena-Pöldsepp E, Sarapuu A, Zulevi B, Kikas A, Piirsoo H-M, Tamm A, Kisand V, Holdcroft S, Serov A, Tammaveski K (2021) Mesoporous iron-nitrogen co-doped carbon materials as cathode catalyst for the anion exchange membrane fuel cell. *J Power Sources Adv* 8:100052–100057
- [32] Alemany-Molina G, Baglio V, Campagna Zignani S, Aticò AS, Morallón E, Cazorla-Amorós D, Lo Vecchio C (2025) Fe-N_x biomass-derived carbon material as efficient cathode electrocatalyst for alkaline direct methanol fuel cells. *Chem Eng J* 505:159655–159662
- [33] Qiao Z, Wang C, Li C, Zeng Y, Hwang S, Li B, Karakalos S, Park J, Kropf AJ, Wegener EC, Gong Q, Xu H, Wang G, Myers DJ, Xie J, Spindelow JS, Wu G (2021) Atomically dispersed single iron sites for promoting Pt and Pt₃Co fuel cell catalysts: performance and durability improvements. *Energy Environ Sci* 14:4948–4960
- [34] Liang L, Jin H, Zhou H, Liu B, Hu C, Chen D, Wang Z, Hu Z, Zhao Y, Li H-W, He D, Mu S (2021) Cobalt single atom site isolated Pt nanoparticles for efficient ORR and HER in acid media. *Nano Energy* 88:106221–106229
- [35] Liang L, Jin H, Zhou H, Liu B, Hu C, Chen D, Zhu J, Wang Z, Li H-W, Liu S, He D, Mu S (2022) Ultra-small platinum nanoparticles segregated by nickel sites for efficient ORR and HER processes. *J Energy Chem* 65:48–54
- [36] Wang F, Liu X, Jiang B, Zhuo H, Chen W, Chen Y, Li X (2023) Low-loading Pt nanoparticles combined with the atomically dispersed FeN₄ sites supported by Fe_{SA}-N-C for improved activity and stability towards oxygen reduction reaction/hydrogen evolution reaction in acid and alkaline media. *J Colloid Interface Sci* 635:514–523
- [37] Pacuła A, Uosaki K, Socha RP, Bielańska E, Pietrzyk P, Zimowska M (2016) Nitrogen-doped carbon materials derived from acetonitrile and Mg–Co–Al layered double hydroxides as electrocatalysts for oxygen reduction reaction. *Electrochim Acta* 212:47–58
- [38] Pei B, Wang W, Dunne N, Li X (2019) Applications of carbon nanotubes in bone tissue regeneration and engineering: superiority. *Concerns, Curr Adv Prospect Nanomater* 9(1501):1–39
- [39] Peng Z, Zhao T, Zhou Y, Li S, Li J, Leblanc RM (2020) Bone tissue engineering via carbon-based nanomaterials. *Adv Healthcare Mater* 9:1901495–1901524
- [40] Arumugam S, Ju Y (2021) Carbon nanotubes reinforced with natural/synthetic polymers to mimic the extracellular matrices of bone—a review. *Mater Today Chem* 20:100420–100441
- [41] Dixon DT, Gomillion CT (2022) Conductive scaffolds for bone tissue engineering: current state and future outlook. *J Funct Biomater* 13(1):1–23
- [42] Arambula-Maldonado R, Mequanint K (2022) Carbon-based electrically conductive materials for bone repair and regeneration. *Mater Adv* 3:5186–5206

- [43] Woodruff MA, Hutmacher DW (2010) The return of a forgotten polymer—polycaprolactone in the 21st century. *Prog Polym Sci* 35:1217–1256
- [44] Kołodziej A, Wesełucha-Birczyńska A, Świętek M, Skalniak Ł, Błażewicz M (2020) A 2D-Raman correlation spectroscopy study of the interaction of the polymer nanocomposites with carbon nanotubes and human osteoblast-like cells interface. *J Mol Struct* 1212:12135–12144
- [45] Wesełucha-Birczyńska A, Kołodziej A, Świętek M, Moskal P, Skalniak Ł, Długoń E, Błażewicz M (2020) Does 2D correlation Raman spectroscopy distinguish polymer nanomaterials due to the nanoaddition? *J Mol Struct* 1217:128342–128347
- [46] Wesełucha-Birczyńska A, Kołodziej A, Świętek M, Skalniak Ł, Długoń E, Pajda M, Błażewicz M (2021) Early recognition of the PCL/fibrous carbon nanocomposites interaction with osteoblast-like cells by Raman spectroscopy. *Nanomater* 11:2890–2908
- [47] Huang B, Vyas C, Roberts I, Poutrel Q-A, Chiang W-H, Blaker JJ, Huang Z, Bártolo P (2019) Fabrication and characterisation of 3D printed MWCNT composite porous scaffolds for bone regeneration. *Mat Sci Eng C* 98:266–278
- [48] Huang B, Vyas C, Byun JJ, El-Newehy M, Huang Z, Bártolo P (2020) Aligned multi-walled carbon nanotubes with nanohydroxyapatite in a 3D printed polycaprolactone scaffold osteogenic differentiation. *Mat Sci Eng C* 108:110374–110384
- [49] e Silva EP, Huang B, Helaehil JV, Nalesso PRL, Bagne L, de Oliveira MA, Albiavetti GCC, Aldalbahi A, El-Newehy M, Santamaria M, Mendonça FAS, Bártolo P, Caetano GF (2021) Caetano, in vivo study of conductive 3D printed PCL/MWCNTs scaffolds with electrical stimulation for bone tissue engineering. *J Bio-Design Manuf* 4:190–202
- [50] Gonçalves EM, Oliveira FJ, Silva RF, Neto MA, Fernandes MH, Amaral M, Vallet-Regí M, Vila M (2016) Three-dimensional printed PCL-hydroxyapatite scaffolds filled with CNTs for bone cell growth stimulation. *J Biomed Mater Res B Appl Biomater* 104B:1210–1219
- [51] Mohammadpour S, Mokhtarzade A, Jafari-Ramani A, Solati-Hashjin M (2024) Tailoring surface properties of poly(caprolactone)/hydroxyapatite scaffolds through aminolysis and multi-walled carbon nanotube coating for bone tissue engineering. *Mater Today Commun* 39:109056–109072
- [52] Pacuła A, Ikeda K, Masuda T, Uosaki K (2012) Examination of the electroactive composites containing cobalt nanoclusters and nitrogen-doped nanostructured carbon as electrocatalysts for oxygen reduction reaction. *J Power Sources* 220:20–30
- [53] Bigall NC, Härtling T, Klose M, Simon P, Eng LM, Eychmüller A (2008) Monodisperse platinum nanospheres with adjustable diameters from 10 to 100 nm: synthesis and distinct optical properties. *Nano Lett* 8:4588–4592
- [54] Diban N, Sánchez-González S, Lázaro-Diez M, Ramos-Vivas J, Urtiga A (2017) Facile fabrication of poly(ϵ -caprolactone)/graphene oxide membranes for bioreactors in tissue engineering. *J Membr Sci* 540:219–228
- [55] Świętek M, Broż A, Kołodziej A, Hodan J, Tokarz W, Hlukhaniuuk A, Wesełucha-Birczyńska A, Bačáková L, Horák D (2022) Magnetic poly(ϵ -caprolactone)-based nanocomposite membranes for bone cell engineering. *J Magn Magn Mater* 563:169967–169977
- [56] Kwon Y, Kim K, Ryoo R (2016) N-doped zeolite-templated carbon as metal-free electrocatalyst for oxygen reduction. *RSC Adv* 6:43091–43097
- [57] Valente JS, Sánchez-Cantú M, Lima E, Figueras F (2009) Method for large-scale production of multimetallic layered double hydroxides: formation mechanism discernment. *Chem Mater* 21:5809–5818
- [58] Hao S, Qian L, Wu Q, Li D, Han F, Feng L, Xin L, Yang T, Wang S, Zhang J, He M (2022) Subnanometer single-walled carbon nanotube growth from Fe-containing layered double hydroxides. *Chem Eng J* 446:137087–137093
- [59] Koyejo AO, Kesavan L, Damlin P, Salomäki M, Kvarnström C (2022) Synthesis of layered double hydroxides and TiO_2 supported metal nanoparticles for electrocatalysis. *Chem Electro Chem* 9:e202200442–e202200452
- [60] Fruehan RJ (1977) The rate of reduction of iron oxides with carbon. *Metall Trans B* 8:279–286
- [61] Krishnakutty N, Rodriguez NM, Baker RTK (1996) Effect of copper on the decomposition of ethylene over an iron catalyst. *J Catal* 158:217–227
- [62] Choi CH, Park SH, Woo SI (2012) Facile growth of N-doped CNTs on Vulcan carbon and the effects of iron content on electrochemical activity for oxygen reduction reaction. *Int J Hydrogen Energy* 37:4563–4570
- [63] Biscoe J, Warren BE (1942) An X-ray study of carbon black. *J Appl Phys* 13:364–371
- [64] Charretier F, Jaouen F, Ruggeri S, Dodelet J-P (2008) Fe/N/C/non-precious catalysts for PEM fuel cells: Influence of the structural parameters of pristine commercial carbon blacks on their activity for oxygen reduction. *Electrochim Acta* 53:2925–2938
- [65] Sadezky A, Muckenhuber H, Grothe H, Niessner R, Poschl U (2005) Raman microspectroscopy of soot and related carbonaceous materials: spectral analysis and structural information. *Carbon* 43:1731–1742
- [66] Yang H, Wang H, Ji S, Linkov V, Wang R (2014) Synergy between isolated- Fe_3O_4 nanoparticles and CN_x layers derived from lysine to improve the catalytic activity for oxygen reduction reaction. *Int J Hydrogen Energy* 39:3739–3745
- [67] Biddinger EJ, Ozkan US (2010) Role of graphitic edge plane exposure in carbon nanostructures for oxygen reduction reaction. *J Phys Chem C* 114:15306–15314
- [68] Sjoström H, Stafström S, Boman M, Sundgren J-E (1995) Superhard and elastic carbon nitride thin films having fullerene-like microstructure. *Phys Rev Lett* 75:1336–1339
- [69] Pels JR, Kapteijn F, Moulijn JA, Zhu Q, Thomas KM (1995) Evolution of nitrogen functionalities in carbonaceous materials during pyrolysis. *Carbon* 33(11):1641–1653
- [70] Macdonald DD, Owen D (1973) The electrochemistry of iron in 1M lithium hydroxide solution at 22 and 200 °C. *J Electrochem Soc* 120(3):317–324
- [71] Ujimine K, Tsutsumi A (2006) Electrochemical characteristics of iron carbide as an active material in alkaline batteries. *J Power Sources* 160:1431–1435
- [72] Wu Z-S, Yang S, Sun Y, Parvez K, Feng X, Müllen K (2012) 3D nitrogen-doped graphene aerogel-supported F_3O_4 nanoparticles as efficient electrocatalysts for the oxygen reduction reaction. *J Am Chem Soc* 134:9082–9085
- [73] Zielke U, Hüttinger KJ, Hoffman WP (1996) Surface-oxidized carbon fibers: I. Surface structure and chemistry. *Carbon* 34:983–998
- [74] Biniak S, Szymański G, Siedlewski J, Świątkowski A (1997) The characterization of activated carbons with oxygen and nitrogen surface groups. *Carbon* 35:1799–1810
- [75] László K, Tombác E, Josepovits K (2001) Effect of activation on the surface chemistry of carbons from polymer precursors. *Carbon* 39:1217–1228

- [76] Jiménez Mateos JM, Fierro JLG (1996) X-ray photoelectron spectroscopic study of petroleum fuel cokes. *Sur Interface Anal* 24:223–236
- [77] Thommes M, Kaneko K, Neimark AV, Olivier JP, Rodriguez-Reinoso F, Rouquerol J, Sing KSW (2015) Physisorption of gases, with special reference to the evaluation of surface area and pore size distribution (IUPAC Technical Report). *Pure Appl Chem* 87:1051–1069
- [78] Jiang Y, Yang L, Sun T, Zhao J, Lyu Z, Zhuo O, Wang X, Wu Q, Ma J, Hu Z (2015) Significant contribution of intrinsic carbon defects to oxygen reduction activity. *ACS Catal* 5:6707–6712
- [79] Kabir S, Artyushkova K, Serov A, Atanassov P (2018) Role of nitrogen moieties in N-doped 3D-graphene nanosheets for oxygen electroreduction in acidic and alkaline media. *ACS Appl Mater Interfaces* 10:11623–11632
- [80] Han SW, Bang J, Ko SH, Ryoo R (2019) Variation of nitrogen species in zeolite-templated carbon by low-temperature carbonization of pyrrole and the effect on oxygen reduction activity. *J Mater Chem A* 7:8353–8360
- [81] Zhang L, Kim J, Dy E, Ban S, Tsay K-C, Kawai H, Shi Z, Zhang J (2013) Effect of template size on the synthesis of mesoporous carbon spheres and their supported Fe-based ORR electrocatalysts. *Electrochim Acta* 108:814–819
- [82] Chen S, Bi J, Zhao Y, Yang L, Zhang C, Ma Y, Wu Q, Wang X, Hu Z (2012) Nitrogen-doped carbon nanocages as efficient metal-free electrocatalysts for oxygen reduction reaction. *Adv Mater* 24:5593–5597
- [83] Tao G, Zhang L, Chen L, Cui X, Hua Z, Wang M, Wang J, Chen Y, Shi J (2015) N-doped hierarchically macro/mesoporous carbon with excellent electrocatalytic activity and durability for oxygen reduction reaction. *Carbon* 86:108–117
- [84] Zhao H, Li L, Liu Y, Geng X, Yang H, Sun C, An B (2020) Synthesis and ORR performance of nitrogen-doped ordered microporous carbon by CVD of acetonitrile vapor using silanized zeolite as template. *Appl Surf Sci* 504:144438–144446
- [85] Pacuła A, Socha RP, Pietrzyk P, Zimowska M, Ruggiero-Mikołajczyk M, Mucha D, Kosydar R, Mordarski G (2018) Physicochemical and electrochemical properties of the carbon materials containing nitrogen and cobalt derived from acetonitrile and Co-Al layered double hydroxides. *J Mater Sci* 53(16):11292–11314
- [86] Tran T-N, Song MY, Singh KP, Yang D-S, Yu J-S (2016) Iron-porphyrrole electrocatalyst with remarkable activity and stability for ORR in both alkaline and acidic conditions: a comprehensive assessment of catalyst preparation sequence. *J Mater Chem A* 4:8645–8657
- [87] Kumar RS, Mannu P, Prabhakaran S, Nga TTT, Kim Y, Kim DH, Chen J-L, Dong C-L, Yoo DJ (2023) Trimetallic oxide electrocatalyst for advanced redox activity in zinc-air batteries evaluated by in-situ analysis. *Adv Sci* 10:2303525–2303539
- [88] Chaudhari NK, Song MY, Yu J-S (2014) Heteroatom-doped highly porous carbon from human urine. *Sci Rep* 4:5221–5230
- [89] Li Y, Zhou W, Wang H, Xie L, Liang Y, Wei F, Idrobo J-C, Pennycook SJ, Dai H (2012) An oxygen reduction electrocatalyst based on carbon nanotube-graphene complexes. *Nat Nanotechnol* 7:394–400
- [90] Deng D, Yu L, Wang G, Jin L, Pan X, Deng J, Sun G, Bao X (2013) Iron encapsulated within pod-like carbon nanotubes for oxygen reduction reaction. *Angew Chem Int Ed* 52:371–375
- [91] Jiang W-J, Gu L, Li L, Zhang Y, Zhang X, Zhang L-J, Wang J-Q, Hu J-S, Wei Z, Wan L-J (2016) Understanding the high activity of Fe-N-C electrocatalysts in oxygen reduction: Fe/Fe₃C nanoparticles boost the activity of Fe-N_x. *J Am Chem Soc* 138:3570–3578
- [92] Mecerreyes D, Stevens R, Nguyen C, Pomposo JA, Bengoetxea M, Grande H (2002) Synthesis and characterization of polypyrrole-graft-poly(ϵ -caprolactone) copolymers: new electrically conductive nanocomposites. *Synth Met* 126:173–178
- [93] Yousefi N, Sun X, Lin X, Shen X, Jia J, Zhang B, Tang B, Chan M, Kim J-K (2014) Highly aligned graphene/polymer nanocomposites with excellent dielectric properties for high-performance electromagnetic interface shielding. *Adv Mater* 26:5480–5487
- [94] Sánchez-Romate XF, Artigas J, Jiménez-Suárez A, Sánchez M, Güemes A, Ureña A (2019) Critical parameters of carbon nanotube reinforced composites for structural health monitoring applications: Empirical results versus theoretical predictions. *Compos Sci Technol* 171:44–53
- [95] Samet M, Kallel A, Serghei A (2022) Maxwell-Wagner-Sillars interfacial polarization in dielectric spectra of composite materials: scaling laws and applications. *J Comp Mater* 56:3197–3217
- [96] Zhao X, Koos AA, Chu BTT, Johnston C, Grobert N, Grant PS (2009) Spray deposited fluoropolymer/multi-walled carbon nanotube composite films with high dielectric permittivity at low percolation threshold. *Carbon* 47:561–569
- [97] Wu TM, Chen EC (2006) Crystallization behavior of poly(ϵ -caprolactone)/multiwalled carbon nanotube composites. *J Polym Sci Part B Polym Phys* 44:598–606
- [98] Fadaie M, Mirzaei E (2018) Nanofibrillated chitosan/polycaprolactone bionanocomposite scaffold with improved tensile strength and cellular behaviour. *Nanomed J* 5(2):77–89
- [99] Lyu JS, Lee J-S, Han J (2019) Development of a biodegradable polycaprolactone film incorporated with an antimicrobial agent via an extrusion process. *Sci Rep* 9:20236–20246
- [100] Bagheri M, Mahmoodzadeh A (2020) Polycaprolactone/graphene nanocomposites: synthesis, characterization and mechanical properties of electrospun nanofibers. *J Inorg Organometallic Polym Mater* 30:1566–1577
- [101] Holešová S, Barabaszová KČ, Hundáková M, Ščuková M, Hrabovská K, Jozsko K, Antonowicz M, Gzik-Zroska B (2021) Development of novel thin polycaprolactone (PCL)/clay nanocomposite films with antimicrobial activity promoted by the study of mechanical, thermal, and surface properties. *Polymers* 13:3193–3212
- [102] Ma J, Zhang S, Qi Z, Li G, Hu Y (2002) Crystallization behaviors of polypropylene/montmorillonite nanocomposites. *J Appl Polym Sci* 83:1978–1985
- [103] He F, Lau S, Laiwa Chan H, Fan J (2009) High dielectric permittivity and low percolation threshold in nanocomposites based on poly(vinylidene fluoride) and exfoliated graphite nanoplates. *Adv Mater* 21:710–715
- [104] Saeed K, Park S-Y (2007) Preparation and properties of multi-walled carbon nanotube/polycaprolactone nanocomposites. *J Appl Polym Sci* 104:1957–1963
- [105] Meng L, Jiang A, Chen R, Li CZ, Wang L, Qu Y, Wang P, Zhao Y, Chen C (2013) Inhibitory effects of multiwall carbon nanotubes with high iron impurity on viability and neuronal differentiation in cultured PC12 cells. *Toxicology* 313:49–58
- [106] Valentini L, Cardinali M, Kenny J (2014) Flexible triboelectric generator and pressure sensor based on poly[(R)-3-hydroxybutyric acid] biopolymer. *J Polym Sci B Polym Phys* 52:859–863

- [107] Elzein T, Nasser-Eddine M, Delaite C, Bistac S, Dumas P (2004) FTIR study of polycaprolactone chain organization at interface. *J Colloid Interface Sci* 273:381–387
- [108] Choi J-H, Jegal J, Kim W-N (2006) Fabrication and characterization of multi-walled carbon nanotubes/polymer blend membranes. *J Membr Sci* 284:406–415
- [109] Flores-Cedillo ML, Alvarado-Estrada KN, Pozos-Guillén AJ, Murguía-Ibarra JS, Vidal MA, Cervantes-Uc JM, Rosales-Ibáñez R, Cauich-Rodríguez JV (2016) Multiwall carbon nanotubes/polycaprolactone scaffolds seeded with human dental pulp stem cells for bone tissue regeneration. *J Mater Sci Mater Med* 27:35–46
- [110] Mantecón-Oria M, Tapia O, Lafarga M, Berciano MT, Munuera JM, Villar-Rodil S, Paredes JI, Rivero MJ, Diban N, Utriaga A (2022) Influence of the properties of different graphene-based nanomaterials dispersed in polycaprolactone membranes. *Sci Rep* 12:13408–13422
- [111] Świątek M, Tokarz W, Benko A, Nocuń M, Mázl-Chánová E, Błażewicz M (2019) Fabrication of CNT/ION hybrids and their impact on the biomedical applicability of PCL-based composite films. *Polym Comp* 40:E1818–E1830

Publisher's Note Springer Nature remains neutral with regard to jurisdictional claims in published maps and institutional affiliations.